Princeton Plasma Physics Laboratory

PPPL- 4693

PPPL- 4693

Recent Progress Toward an Advanced Spherical Torus Operating Point in NSTX

Stefan Gerhardt, et. al.

October, 2011

PPPL PRINCETON PLASMA PHYSICS LABORATORY

Prepared for the U.S. Department of Energy under Contract DE-AC02-09CH11466.

Princeton Plasma Physics Laboratory
Report Disclaimers

Full Legal Disclaimer

Trademark Disclaimer

PPPL Report Availability

Princeton Plasma Physics Laboratory:

http://www.pppl.gov/techreports.cfm

Office of Scientific and Technical Information (OSTI):

http://www.osti.gov/bridge

Related Links:

U.S. Department of Energy

Office of Scientific and Technical Information

Fusion Links

Recent Progress Toward an Advanced Spherical Torus Operating Point in NSTX

S.P. Gerhardt 1), D. A Gates 1), S.M. Kaye 1), R. Maingi 2), J.E. Menard 1), S.A. Sabbagh 3), V. Soukhanovskii 4), M. G. Bell 1), R.E. Bell 1), J.M. Canik 3), E. Fredrickson 1), R. Kaita 1), E. Kolemen 1), H. Kugel 1), B. P. Le Blanc 1), D. Mastrovito 1), D. Mueller 1), H. Yuh 5)

1) Princeton Plasma Physics Laboratory.
2) Oak Ridge National Laboratory.
3) Department of Applied Physics, Columbia University.
4) Lawrence Livermore National Laboratory.
5) Nova Photonics, Princeton, New Jersey.

Abstract. Progress in the development of integrated advanced ST plasma scenarios in NSTX [M. Ono, et al., Nuclear Fusion **40**, 557 (2000)] is reported. Recent high-performance plasmas in NSTX following lithium coating of the plasma facing surfaces have achieved higher elongation and lower internal inductance than previously. Analysis of the thermal confinement in these lithiumized discharges shows a stronger plasma current and weaker toroidal field dependence than in previous ST confinement scaling studies; the ITER-98(y,2) scaling expression describes these scenarios reasonable well. Analysis during periods free of MHD activity has shown that the reconstructed current profile can be understood as the sum of pressure driven, inductive, and neutral beam driven currents, without requiring any anomalous fast ion transport. Non-inductive fractions of 65-70%, and β_P>2, have been achieved at lower plasma current. Some of these low-inductance discharges have a significantly reduced no-wall β_N limit, and often have β_N at or near the with-wall limit. Coupled m/n =1/1 + 2/1 kink/tearing modes can limit the sustained β values when rapidly growing ideal modes are avoided. A β_N controller has been commissioned and utilized in sustaining high-performance plasmas. "Snowflake" divertors compatible with high-performance plasmas have been developed. Scenarios with significantly larger aspect ratios have also been developed, in support of next-step ST devices. Overall, these NSTX plasmas have many characteristics required for next-step ST devices.

Keywords: NSTX, Spherical Torus, MHD, Plasma Confinement

PACS #s: 52.55.Fa, 52.55.Tn, 52.55.Wq

E-mail contact of corresponding author: sgerhard@pppl.gov
Address: Princeton Plasma Physics Lab
PO Box 451
Princeton, NJ 08543

Paper Is Associated with the 2010 IAEA FEC in Daejeon, Korea

2 Tables
23 Figures
11 Sections + References

1. Introduction

The spherical torus (ST) [1] has several potential benefits compared to a conventional aspect ratio tokamak. One is the natural elongation (κ) of the plasma cross-section [2], especially when the internal inductance is low [3]. Furthermore, the magnetohydrodynamic (MHD) stability limit on the normalized-β, $\beta_N = \beta_T/(I_p/aB_T)$ (in units %·m·T/MA, with β_T defined in terms of the volume average pressure $\langle p \rangle$ and the toroidal magnetic field on axis) is higher at low aspect ratio [3-5]. The combination of the low aspect ratio $A = R_0/a$, the natural elongation and the higher β_N facilitates operation at very high toroidal β, since Troyon scaling [6,7] implies $\beta_T = \beta_N \times (I_p/aB_T) \propto \beta_N \kappa/Aq$. In addition, the compact configuration of the ST facilitates remote maintenance [8-11].

For these reasons, the ST has been suggested as the fusion core configuration for both fusion reactors and fusion technology development [9,12,13]. As a reactor [14,15,16], the current drive power must be minimized; this mandates that $\beta_P = 2\mu_0\langle p \rangle / B_p^2$ must be very high, since the bootstrap fraction scales with β_P [3,4]. The toroidal β must be high, since the fusion power scales as β_t^2 and the dissipation in the (typically normally conducting [15]) toroidal field coil must be minimized. The device would thus need to operate at simultaneously high κ and β_N, since the product $\beta_P\beta_T$ is proportional to $\left(1+\kappa^2\right)\beta_N^2$ [3,4]. Typical values of these parameters in reactor studies are $\kappa = 3.0 - 3.2$ and $\beta_N \approx 8$. As a device to study plasma material interactions [17] or nuclear technology [8-11,13,18,19] a substantial fraction ($30 - 50\%$) of the current can be provided by circulating unthermalized ions from injected neutral beams. This relaxes the equilibrium requirements somewhat, though reasonably high elongation ($2.5 - 3$) and β_N ($3.5 - 4.5$) are still required.

The excellent progress in ST research over the past 15-20 years provides evidence that devices with these parameters are within reach. The physics merits of the ST configuration, as described in papers such as Peng and Strickler [1], were first observed in the START (Small Tight Aspect Ratio Torus) device [20]. The low aspect ratio and strong shaping achieved in this device allowed operation at high normalized current $I_N = I_P/aB_T$, with a then world record $\beta_T \approx 30\%$ [21,22]. Computational studies from the same period further demonstrated the potential of the spherical torus configuration [3,4]. For instance, the study by Menard, et al. [3] found $\kappa = 3$, $\beta_T = 45\%$ configurations stable to $n = 1$, 2 & 3 kink and $n = \infty$ ballooning instabilities in the presence of a nearby conducting wall. Greater than 99% of the toroidal current in this equilibria was self-driven by the bootstrap effect.

The results described above motivated and guided the physics and engineering design of two 1 MA class STs: the National Spherical Torus Experiment (NSTX) [23] and the Mega-Ampere Spherical Torus (MAST) [24]. These devices have confirmed many of the attractive characteristics of the ST on a larger scale, including the achievements of H-modes [25,26] with good confinement [27-29], transient toroidal β of ~35% [30,31] (transient in this context implies a configuration that is sustained for less

than an energy confinement time) and β_N in the range $5-6$ [5,30-42]. These achievements are important steps toward the devices described above.

This paper describes progress in developing plasmas in NSTX [23] designed to study the characteristics of high-elongation, high–β scenarios sustained for durations longer than a current redistribution time, guided by the needs of next-step ST designs. Section 2 contains a description of the NSTX device and the analysis techniques used in this paper. Section 3 presents the time evolution of a few example discharges, including comparison to high-performance discharges reported in previous papers. Section 4 presents database analysis of NSTX parameters; both global stability and transport are discussed. Section 5 presents analysis of the current profile and non-inductive fraction, and a discussion regarding magnetohydrodynamic (MHD) stability and control is given in section 6. Section 7 contains a discussion of the extrapolability of these scenarios to steady state. Section 8 briefly describes research into advanced divertors in high-performance plasmas, while section 9 describes the performance of plasmas with higher aspect ratio produced in NSTX. A discussion and summary of these results is given in section 10. This paper is an update on the discussion presented in two previous papers [43,44], and on previous NSTX scenario development described by Gates [45,46] and Menard [35].

2. The NSTX Device and Relevant Analysis Techniques.

NSTX is a medium sized spherical tokamak with typical plasma major radius $R_0 \approx 0.85$ m and minor radius $a \approx 0.6$ m (here, we define $R_0 = \left(R_{mid,out} + R_{mid,in}\right)/2$ and $a = \left(R_{mid,out} - R_{mid,in}\right)/2$, where $R_{mid,in}$ & $R_{mid,in}$ are the midplane intersection radii of the inboard and outboard plasma boundary). A plasma cross-section with an elongation $\kappa \approx 2.5$ optimally fills the vessel, although higher values are possible. Plasma currents range from 0.6 to 1.3 MA and toroidal fields from 0.35 to 0.55 T; operation at smaller values of these parameters is possible but uncommon. Auxiliary plasma heating is provided by up to 7.5 MW of co-injected neutral beams (NBs) and up to 6 MW of 30 MHz high-harmonic fast wave (HHFW) heating; the discharges in this paper use NB heating only. A flexible digital control system [47,48] provides a means to control the plasma shape [49], non-axisymmetric field perturbations, and heating sources. Upgrades to the plasma control computer in 2008 reduced the system latency by a factor of 5, from ~3 msec to 0.6 msec) [48]. This increased "responsiveness" of the system is important for facilitating the high-elongation operation described in this paper.

Lithium conditioning of the plasma facing components (PFCs) has been used for virtually all high-performance discharge development in NSTX in the 2008-2010 campaigns. The lithium is introduced into the machine prior to each discharge via a dual evaporator system [50]. The evaporators are directed toward the graphite tiles of the lower divertor, where the evaporated lithium forms a solid coating; some lithium is also deposited on the center column, lower passive plates, and vessel inner walls (see references [50] and [51] for additional information on the distribution toroidal and poloidal distribution of the evaporated lithium). The use of lithium in this way has been

shown to lower the H-mode threshold [52,53], reduce or eliminate ELMs [54], reduce deuterium recycling [55], improve confinement [51,56], and reduce the internal inductance [51]. However, the elimination of ELMs also results in good particle confinement, so that impurity accumulation can pose an issue in these ELM-free discharges. Typical lithium deposition amounts for scenario development experiments are 200 – 300 mg before each discharge.

A third important improvement (along with PCS latency reduction and lithium PFC conditioning) has been, starting mid-way through the 2008 run-campaign [41], the routine use of active error field correction and $n = 1$ resistive wall mode (RWM) [57] feedback. NSTX is equipped with a set of midplane radial field coils [58], which are typically configured so as to apply $n = 1$ radial fields of arbitrary phase and $n = 3$ fields in one of two phases. It has been found that one of the two available $n = 3$ phases is favorable for maintaining the plasma rotation [39], and that this phase is the one which approximately cancels a known $n = 3$ error field due to a non-circularity in the main vertical field coil [40]. We use a feedback system with internal poloidal and radial field sensors and the midplane radial field coils for $n = 1$ control. The $n = 1$ component of the intrinsic NSTX error field is corrected via the slowly varying fields applied by the feedback system [39]. Fast growing resistive wall modes are suppressed by the higher-frequency response of the system [36]. This system has proven to improve the reliability of high performance NSTX scenarios [41], and the most recent progress in this area is summarized by Sabbagh [42]. Note also that NSTX has four rows of copper stabilizing plates, two above and two below the midplane, which, when combined with plasma rotation, can passively stabilize the RWM [34,37,38].

We note that these improvements interact in important ways. For instance, section 4.1 will illustrate the importance of strong shaping in sustaining high β_N; this strong shaping is facilitated by the reduced PCS latency (enabling a faster vertical control response) and lithium conditioning by reducing the internal inductance. Similarly, the improved confinement provided by lithium conditioning can be better exploited when the n=1 feedback systems and strong shaping provide stable access to higher β_N.

Equilibrium reconstruction, i.e. finding the solution to the Grad-Shafranov equation [58] that is most consistent with the available diagnostic data, is an important part of this analysis. Many results presented in this paper come from “partial kinetic” reconstructions performed with the EFIT code [37,59], which are automatically generated for each discharge and are constrained by external magnetics, the measured plasma diamagnetism, and a loose constraint on the pressure profile (the measured electron pressure profile, and approximate thermal and fast ion pressure profiles with large error bars, are used to approximately constrain the MHD pressure profile while allowing sufficient freedom to fit a range of profiles, see Ref. [37]). When more detailed equilibrium analysis is required, the LRDFIT code [35] has been used. These reconstructions are constrained by external magnetics, the plasma diamagnetism, the pitch angle measurements from up to 16 channels of motional Stark effect polarimetry [60], and the requirement that the temperature on the inboard and outboard midplane of a given magnetic surface be the same (the NSTX 30 channel Thomson scattering system

[61] is located at the midplane and measures both inboard and outboard sides of the profiles).

We typically use the TRANSP code [62] to compute quantities such as the confinement parameters and non-inductive fractions, using the measured electron and ion temperatures, electron and carbon density profiles, and carbon toroidal rotation. The deuterium density profile is inferred from quasi-neutrality. We typically use the Sauter formulation [63] in TRANSP to compute the bootstrap current profile and total pressure driven current level. The neutral beam heating and current drive is computed with the NUBEAM module [64] within TRANSP. The analysis of experimental data is typically done by imposing the magnetic geometry and q-profile from the reconstruction codes; however, some modeling in Sect. 7 does solve the poloidal field diffusion equation for the q-profile.

We also utilize calculations of the no-wall and with-wall ideal MHD stability limits in Sections 6 & 9. The calculations are based on the LRDFIT reconstructions. The CHEASE fixed-boundary equilibrium code [65] is used to generate a range of equilibria with scaled pressure profiles. The equilibria are then assessed with the DCON ideal stability code [66], in order to determine the β_N at which the $n = 1$ modes become unstable; this calculation is repeated both with and without the nearby wall.

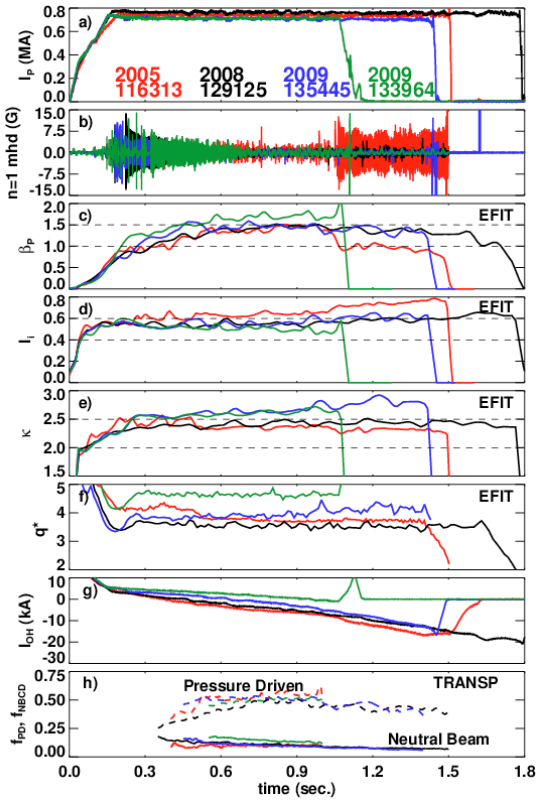

Fig. 1) Comparison of discharges designed to maximize the pulse length or non-inductive fraction. Shown are a) I_P, b) the n=1 MHD trace, c) β_P, d) l_i, e) κ, f) q, g) the solenoid current, and h) the pressure and neutral beam driven current fractions.*

3. Recent Example Discharges at the NSTX Performance Boundary and Comparison to Previous Discharges

We have made substantial progress in the development of high-β sustained plasma scenarios since previous NSTX scenario papers [35,46]. This section compares example recent discharges to previously discussed examples, in order to illustrate where progress has and has not been made.

Fig. 1 shows time traces from discharges designed to operate either with maximum pulse length or minimum non-inductive currents. These are slightly different optimization targets because the large toroidal field (TF) that maximizes β_P (and thus the bootstrap current fraction) limits the pulse length due to TF coil heating. Here, β_P is defined as $\beta_P = 2\mu_0 \langle P \rangle_{Vol} / B_P^2$ with $B_P = \mu_0 I_P / l_{pol}$ with l_{pol} the poloidal circumference of the separatrix. Shown in the figure are the plasma current I_P, the odd-n rotating MHD signature (which is generally dominated by n=1 perturbations), β_P, the internal inductance l_i, the elongation κ, the cylindrical safety factor q^*, the solenoid current, and the pressure- and neutral beam driven current fractions f_{PD} and f_{NBCD}. The pressure driven fraction includes contributions from the bootstrap, Pfirsch-Schlüter, and diamagnetic currents, the internal inductance l_i is defined as $l_i(1) = l_p^2 \iiint B_P^2 dV \Big/ V\left(\mu_0 I_P\right)^2$, and q^* is defined as $q^* = \dfrac{\varepsilon \pi a B_T \left(1+\kappa^2\right)}{\mu_0 I_P}$. This parameter was previously identified as an aspect-ratio independent indicator of the low-q boundary, with $q^* < 1.8$ leading to a rapid degradation in stability [5].

Discharge 116313 (red in Fig. 1), from 2005 and before the advent of error field correction or lithium PFC conditioning, had an NSTX-best pulse length and sustained non-inductive fraction at the time, but succumbed to an m/n = 1/1 rotating MHD mode midway through the discharge [35]. This instability led to substantial rotation braking and confinement loss, ending the high-β phase of the discharge. The lower single null shape of this plasma is illustrated in frame a) of Fig. 2, showing that it has high triangularity, but only moderately high elongation (κ = 2.2 – 2.3).

Discharge 129125 (black in Fig. 1), from 2008, is the longest pulse to date in NSTX, lasting ~300 ms beyond the end of the TF flat-top [39]. This discharge maintains a high-β state through the pulse, with no core-MHD, though the elongation of 2.3 is not significantly larger than the 2005 discharge discussed above. The use of error-field control (for stable operation at higher β_N) and lithium conditioning (for improved confinement and reduced internal inductance) was critical for the development of this and subsequent scenarios.

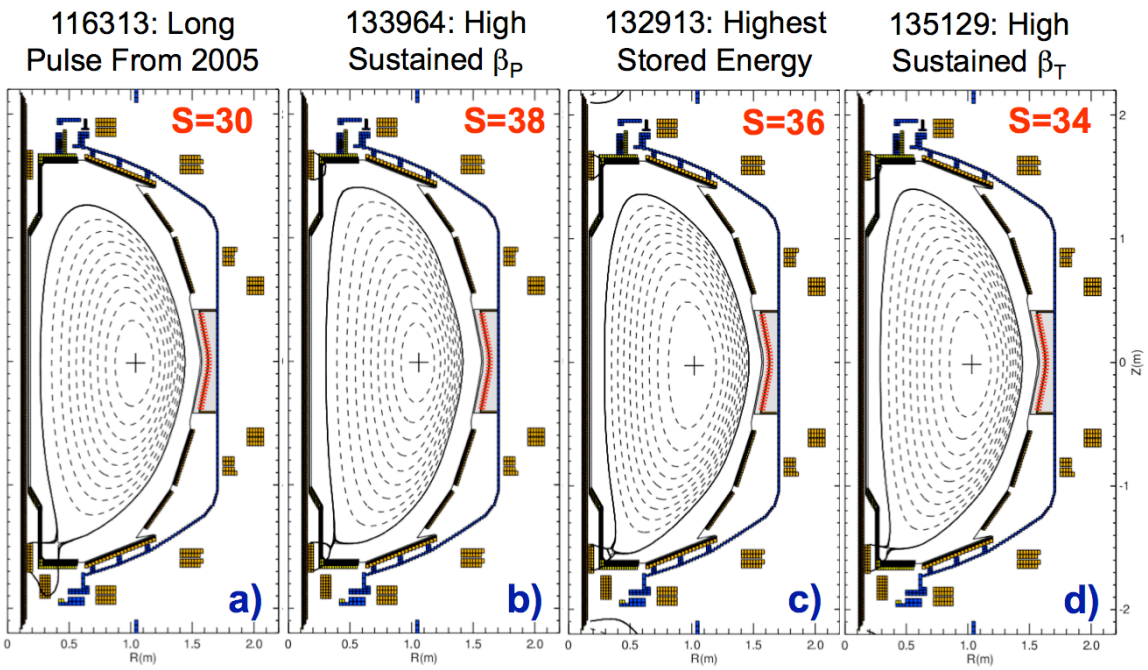

Fig. 2: Plasma boundary shapes for four of the discharges discussed in Figs. 1 & 3. The shape factor S (= $q_{95}I_p/aB_T$) for each case is indicated in red.

The final two discharges in this figure are from the 2009 campaign, and have slightly lower current than those discussed above (0.7 *vs*. 0.75 MA). Discharge 133964 (green) is also operated at increased toroidal field ($B_T = 0.48$ T instead of 0.38 for the others); see Ref. [67] for the first discussion of discharges in this class, and Fig. 2b) for the plasma boundary shape. These recent discharges differ from earlier examples by their higher elongation (2.6 compared to 2.3) and lower internal inductance l_i. Discharge 133964 in particular has a flat-top average surface-voltage of 130 mV, the lowest ever achieved in a beam-heated H-modes in NSTX. Considering the non-inductive fractions in the lowest frame of Fig. 1, we see that 133964 has a neutral beam current drive fraction of ~18% in the early lower-density phase, significantly exceeding that from previous discharges. The pressure-driven current fraction reliably achieves 50% in these scenarios, which is nearly adequate for many next-step device designs [8,9]. The confinement (not shown) is comparable to or better than that expected from $ITER98_{y,2}$ H-mode scaling [68].

The second style of discharge optimization, illustrated in Fig. 3, is to increase the toroidal beta and/or the stored energy. An extreme version of this optimization is shown in the I_p = 1.3 MA, B_T = 0.49 T discharge 132913 (green), which set the present NSTX plasma stored energy record of 460 kJ. This value is confirmed both by the partial-kinetic EFIT analysis and TRANSP calculations based on the measured thermal profiles and modeled fast ion stored energy. This discharge, whose shape is shown in Fig. 2b), was taken soon after lithium conditioning began in 2009, and clearly benefited from the improved confinement that lithium PFC conditioning provides.

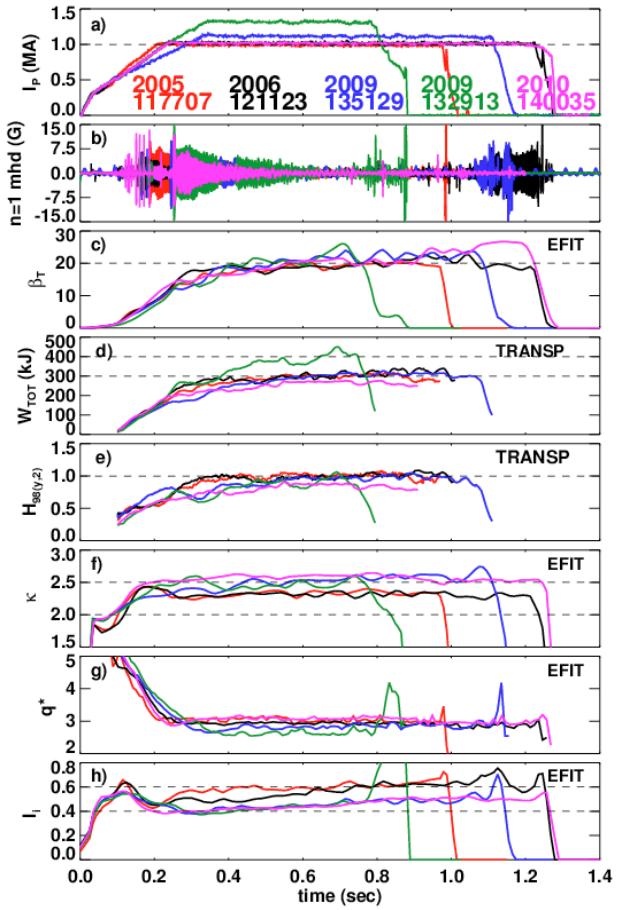

Fig. 3: Comparison of discharges designed to maximize the stored energy or toroidal β. Shown are a) the plasma current, b) the odd-n MHD trace, c) β_T, d) the stored energy, e) the H-mode confinement factor, f) the elongation, g) q, and h) l_i.*

A single 1.1 MA discharge from 2009 (135129 in blue, shape in Fig. 2d), and a series of 1 MA discharges (117707 from 2005 in red, 121123 from 2006 in black, and 140035 from 2010 in magenta) are also shown; these discharges are optimized to maximize the sustainable β_T. Inspection of the figure shows that the most recent discharges maintain comparable or higher β_T values, with significantly higher-elongation (2.5–2.6 compared to 2.2–2.3) and lower l_i (0.4–0.45 compared to 0.55–0.6) compared to previous discharges. Sustained β_T of 22–25% is now common in this class of higher-current discharges. The best 1.0 and 1.1 MA discharges of this type achieve β_N/l_i of 12–14. Also, the most recent 1 MA pulses (like 140035) are able to avoid the onset of any $n = 1$ rotating modes for the duration of the pulse. Again, the confinement is comparable to that predicted by the ITER-98 H-mode scaling expression. We also note that the q^* values for these discharges are at or below 3. In general this class of high-β_T discharge is susceptible to both high-β n=1 instabilities such as the RWM, and rotating n=1 modes that occur as q_{min} evolves towards 1. These instabilities will be discussed in detail in Sect. 6.

The example discharges above show that it has been difficult to achieve large increases in sustained β_T or non-inductive fraction (f_{NI}), compared to previous best

discharges from the 2005-2007 campaigns. Significant progress has been made, however, in developing the high-elongation scenarios and operating stably at reduced internal inductance. Furthermore, as will be shown in the next section, the reliability of these scenarios, as assessed by the duration of sustained high-β and the shot-to-shot reproducibility, has improved dramatically.

4. Analysis of global performance.

4.1: Role of shaping in determining the global performance.

In this section, the progress that has been achieved in the development of sustained high-performance plasmas relevant to next-step devices is substantiated by database analysis. The data in these figures are derived from the partial kinetic EFIT runs that are available for the vast majority of discharges. Each point is the average of a given quantity over the plasma current flat-top, and is thus indicative of the sustainable level; in many cases, this measure underestimates the performance of the discharge, since the stored energy usually reaches its flat-top after the start of the plasma current flat-top. The points are sorted in color by shape factor $S = \frac{q_{95} I_P}{a B_T}$ [69], a parameter previously shown in DIII-D [69], NSTX [46,70], and START [21] to help facilitate high-β operation (note that Fig. 2 has the shape factor for the various shapes indicated in each frame). The symbols in Fig. 4 specify the year of the discharge, as indicated in the legends.

The importance of strong shaping in achieving *sustained* high performance is clearly evident in all cases. For instance, with a single exception, no discharge with a shape factor less than 30 has even maintained a surface voltage less that 0.2 V for any reasonable duration (see frame b). Similarly, $0.5\sqrt{\varepsilon}\beta_P$, a commonly used approximation for the bootstrap current fraction, has only exceeded 0.5 for $S > 30$ (frame d). Although the very highest shaping factor (S>35) has not yet led to very highest β_T and β_N, we have found that increased shaping helps with these two metrics as well.

The figures also show that the 2009 & 2010 NSTX run campaigns produced important expansions in the performance of the device. In particular, virtually all high-performance discharges with $S > 35$ were produced during this period. The discharge regime with $0.5\sqrt{\varepsilon}\beta_P > 0.55$, though first achieved in the 2008 campaign [67], was only fully exploited during this most recent period (here, $\varepsilon = a/R_0 = 1/A$ is the inverse aspect ratio). Similarly, the ability to sustain $\beta_N > 5$ for > 1 second was only recently achieved. Note that, as described in Sect. 2, the reduced PCS system latency and reduced l_i with lithium conditioning played a key role in achieving the strong shaping. Furthermore the shaping and n=1 control facilitated sustainment of the high-β states provided by the improved confinement with lithium conditioning.

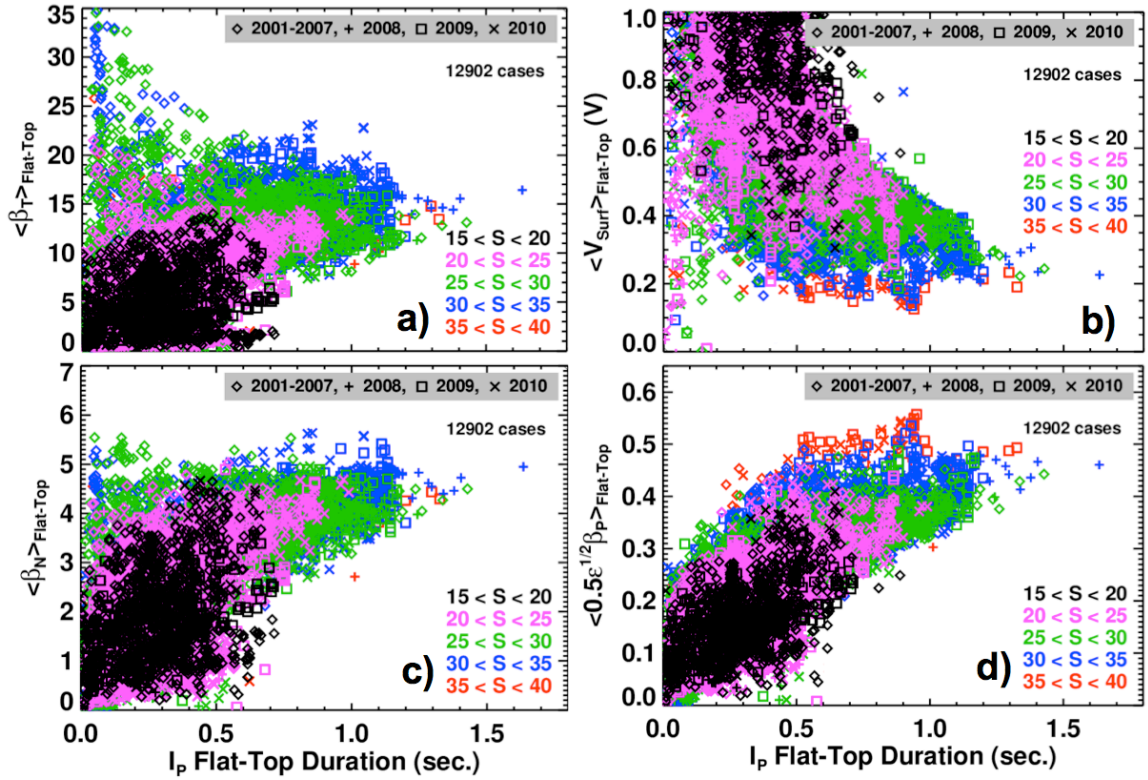

Fig. 4: Flat-top average of global performance parameters plotted against the I_P flat-top duration. The colors represent different values of the shape parameter. The symbols are indicative of the year when the discharge was taken, as indicated in the legend. The quantities shown are a) β_T, b) the surface voltage, c) β_N and d) $0.5\sqrt{\varepsilon}\beta_P$.

4.2 Confinement Scaling in High-Performance Lithiumized Plasmas.

In addition to the large database of equilibrium parameters, we have run the TRANSP code [62] for a large number of high-performance H-mode plasmas, focusing on time windows where there is no low-frequency MHD activity. All discharges in this database benefited from at least some lithium conditioning of the plasma facing components. The database has a wide range of plasma currents (0.5 MA < I_P < 1.3 MA), toroidal fields (0.32 < B_T < 0.54 T), line average densities (3.8×10^{13} < n_e < 9.5×10^{13} cm^{-3}), power (2 < P_{inj} < 6 MW), and elongation (2.0 < κ < 2.8). The chosen time windows have 3.5 < β_N < 6.5, and 0.7 < T_e/T_i < 1.1. The range of $\rho^* = \rho_i/a$ is given by $0.01<\rho^*<0.02$, where ρ_i is defined in terms of the line average ion temperature and vacuum toroidal field. Carbon is typically assumed to be the only impurity, though a few cases use a flat Z_{eff} profile whose time dependence matches that from a single-chord visible bremsstrahlung measurement. Good matches between the measured and simulated stored energy and DD neutron emission have been obtained without the need to invoke anomalous fast-ion diffusion. The time windows for averaging are 60–100 ms long, and are typically at least a current redistribution time past the start of the I_p flat-top. Error bars in this database come from the standard deviation of the quantities within the averaging window. Note that the discharges in this dataset were chosen for their sustained high-β

nature. Many discharges with better confinement were not included, either because the confinement increase led to a β-limit disruption, or because the good confinement was achieved without the strong shaping and sustained high-β that is the focus of this study. This database will be used extensively for studies in this section, as well as Sects. 5, 6, & 9.

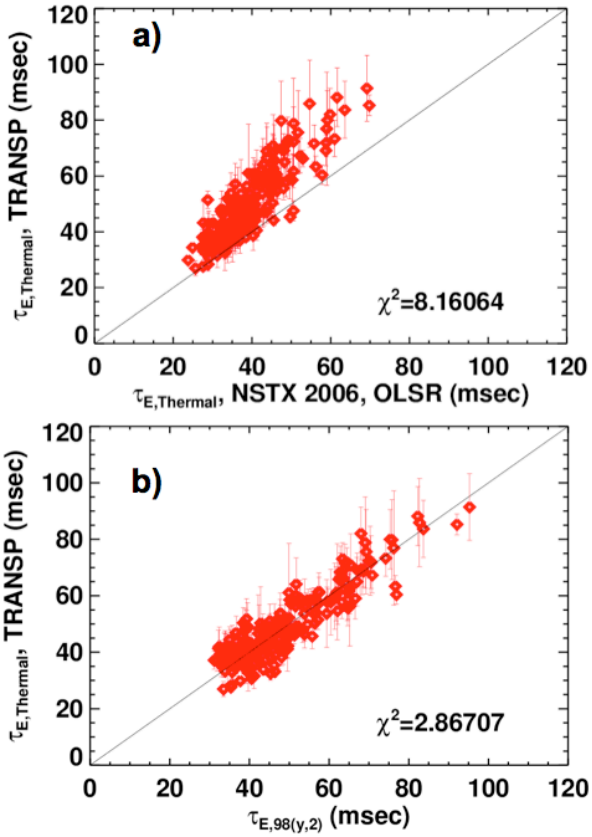

Fig. 5: Thermal confinement times in recent NSTX high performance lithiumized discharges, compared to a) a previously developed NSTX scaling expression, and b) the ITER-98$_{y,2}$ scaling expression.

It is common to compare the achieved confinement time to expectations from scaling expressions of the form $\tau_{E,Thermal} \propto I_P^{\gamma_{I_P}} B_T^{\gamma_{B_T}} n_e^{\gamma_{n_e}} P_L^{\gamma_{P_L}}$ [68]. Here, the loss power P_L is defined as the total heating power (from induction and neutral beams) minus dW_{th}/dt and fast-ion losses due to shine-through, bad-orbit losses, and charge-exchange loss. Fig. 5a) shows the thermal confinement times computed in TRANSP compared to the prediction derived from previous NSTX discharges using an ordinary least squares regression (OLSR) technique: $\tau_{E,Thermal} \propto I_P^{0.57} B_T^{1.08} n_e^{0.44} P_L^{-0.73}$ [28]; the discharges used to generate this scaling expression did not have any lithium conditioning of the plasma facing components. The value of χ^2, defined as $\chi^2 = \frac{1}{N}\sum\left(\frac{\tau_{E,Thermal} - \tau_{scaling}}{\sigma_\tau}\right)^2$, is also shown in the figure, as an indicator of the systematic deviation between the measurements and the

scaled prediction. This expression tends to underestimate the confinement by a factor of 1.25; correcting by this factor reduces χ^2 considerably. Ref. [28] includes a second scaling expression, based on a principal component error-in-variable (PCEIV) method, which results in a scaling $\tau_{E,Thermal} \propto I_P^{0.52} B_T^{0.87} n_e^{0.27} P_L^{-0.5}$. We find that this expression results in a larger deviation from the measured confinement, with a multiplier of 1.4 required.

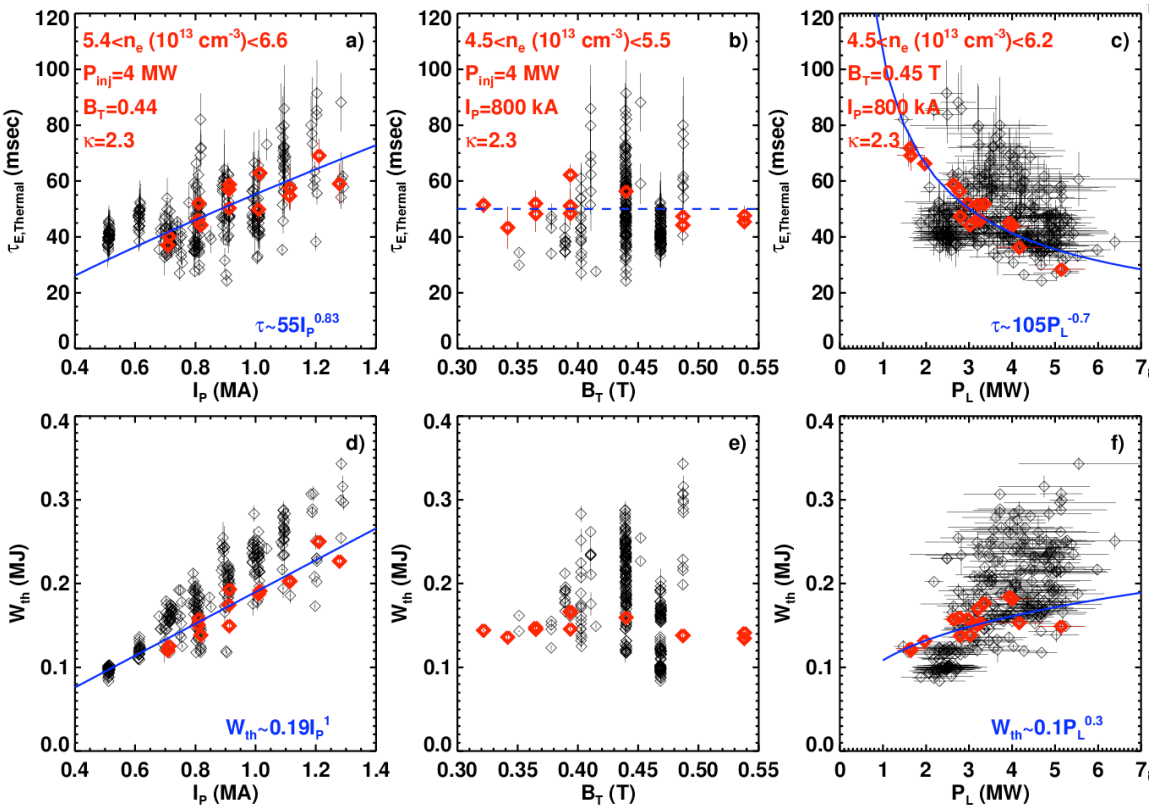

Fig. 6. Results from experiments studying thermal confinement scaling. Shown are a)-c), the dependence of the thermal confinement time on I_P, B_T, and P_L, and d)-e), the thermal stored energy scaling with those same variables. Data from the large TRANSP database is shown in black, and controlled scans in red. Parameters for the controlled scans are shown in red, and simple power law fits to the red points are shown in blue.

Fig. 5b), shows the calculated confinement time for these recent lithium conditioned discharges plotted against the expectation from the ITER98$_{y,2}$ H-mode scaling expression: $\tau_{E,Thermal} \propto I_P^{0.93} B_T^{0.15} n_e^{0.41} P_L^{-0.69}$. The agreement is quite good over a large range of confinement times, with no systematic offsets.

Dedicated scans of I_p, B_T and injected power have been performed in $\kappa = 2.3$ high-performance discharges, each following 300 mg of lithium evaporation. The results of this exercise are shown in Fig. 6), where data from the entire high performance database of TRANSP runs is shown in black, and data from the dedicated scans are shown in red; the parameters of the scans are indicated in red text. Considering the

dedicated single-parameter scans first, we observe in frame a) that the scaling of the thermal confinement time with plasma current is found to be $\gamma_{I_P} \approx 0.85$. This is somewhat stronger than in previous NSTX studies in both NSTX and MAST [29]. More striking was the observation in frame b), showing that there is effectively no dependence of the confinement time on toroidal field, a result common at higher aspect ratio but atypical of previous spherical torus results. The power degradation in frame c) is also found to be strong, with an exponent of $\gamma_{P_L} \approx -0.7$.

These results are corroborated by the plots of thermal stored energy vs. these same variables, shown in frames d-f. We see an essentially linear scaling of the thermal energy with plasma current, and virtually no dependence on toroidal field. The thermal energy has a weak dependence on absorbed power.

We also note that the trends observed in the dedicated scans (in red) are largely duplicated across the entire database (in black). The trends are clearer in the plots of thermal energy in the lower row. We observe a strong increase in stored energy with plasma current, but little systematic dependence on toroidal field. The stored energy increases weakly with absorbed power. Note again that a large range of lithium evaporation rates was used in the larger database, whereas the evaporation rate was maintained at 300 mg/discharge in the dedicated scans.

We have also made regression fits to the larger database of TRANSP runs. This regression analysis has produced an I_p scaling similar to the dedicated scans, with $0.75 < \gamma_{I_P} < 0.9$ being a good fit. This is somewhat stronger than the 2006 scaling OLSR scaling, and much stronger than the PCEIV scaling. The toroidal field scaling from the large database is $0.25 < \gamma_{B_T} < 0.35$, again comparable to the dedicated experiment, but much weaker than that in the previous low-A scaling relationships. Note that because the B_T range in NSTX is small (0.35-0.55 T), the difference in B_T scaling does not appear strongly in the analysis shown in Fig. 5, but is quite clear in Figs. 6 b) and e). The density dependence is generally $0.4 < \gamma_{n_e} < 0.5$, which is again somewhat stronger than the 2006 scaling. The power degradation is quite strong ($-0.8 < \gamma_{P_L} < -0.7$), consistent with the 2006 OLSR scaling, but stronger than the PCEIV result. These values are in general similar to the exponents in the $ITER98_{y,2}$ expression. Inclusion of one or both of κ and the inverse aspect ratio ε in the fit did not change the other exponents significantly or reduce the χ^2 value. However, excluding the density as a regression variable does increase χ^2 and modify the other exponents. Note that these scaling exponents will be used below when discussing the scaling of the bootstrap and neutral beam driven current fraction with engineering variables.

It is interesting to consider why the present results differ from previous ST scaling expressions. A likely reason is the lithium conditioning of the plasma facing components, which is present in all discharges here, but not in the previous NSTX data [27,28]. This lithium conditioning has the effect of modifying the edge pedestal shape [54] and impurity content [51] (which can in turn modify the plasma collisionality). The impact of

these changes on the confinement scaling is a subject under active investigation, and will be reported in a future publication.

5. Current profile analysis and the non-inductive fraction in NSTX.

5.1 Detailed analysis of the current profile.

Part of scenario design for next-step devices includes the optimization the various current drive sources. These include the toroidal part of the Pfirsch-Schlüter and diamagnetic currents [71], the bootstrap current [71-75], currents carried by circulating fast ions injected by the neutral beams [76-78], and inductive currents [79]. It is necessary to have confidence in the models and tools that predict the various current sources. We have made a substantial effort to compare calculations of the current profile constituents to the measured current profile. Those studies are presented in detail in Ref. [80] and are briefly summarized here.

Figure 7 shows a detailed analysis of the current profile for high-performance plasmas at low and high current: a) an $I_p = 0.5$ MA plasma designed to maximize β_P, b) an $I_p = 0.7$ MA high-β_P plasma designed to maximize the non-inductive current fraction, and b) an $I_p = 1.3$ MA plasma designed to maximize the stored energy. The bootstrap current is computed in TRANSP [62] using the Sauter model [63], and the neutral beam current is computed with the NUBEAM code [64]. The inductive current is determined by computing the loop voltage profile from a time-sequence of MSE constrained equilibria [79] and multiplying it by the neoclassical resistivity as computed in the Sauter model [63]. There is no low-frequency MHD activity during the chosen time windows, and no anomalous fast-ion diffusion was used in any of these calculations; there is a good match between the measured and simulated neutron emission rates.

The 0.5 MA example in frame a), which achieved $\beta_P = 2$, illustrates the common features of this analysis in NSTX. The profile shows a characteristic two-hump shape, with the edge feature coming from the edge bootstrap "bump" and inductive currents, and the core feature from the inductive and centrally located beam driven currents. Good agreement is found between the current profile inferred from MSE constrained LRDFIT reconstructions (black) and from summing the individual current constituents (green). This discharge will be discussed again in Sect. 5.4.

For the 0.7 MA case in frame b) (and also described in Figs. 1 & 2c) which had the lowest surface voltage of any NB-heated discharge in NSTX, we see that the loop voltage profile is flat, indicating that the current profile has stopped evolving. Good agreement is again found between the two means of reconstructing the current profile. Finally, for the 1.3 MA case in frame c), we again see agreement in the current profile reconstruction. Note, however, that the loop voltage profile in this case is hollow, indicating that the current has not fully penetrated. Much more detailed analysis and discussion of the non-inductive current profile in NSTX high-performance plasmas can be found in Ref. [80], including a discussion of cases where MHD modes cause fast-ion

redistribution, and an estimate is made of the upper bound on the fast-ion diffusivity in MHD-quiescent regimes.

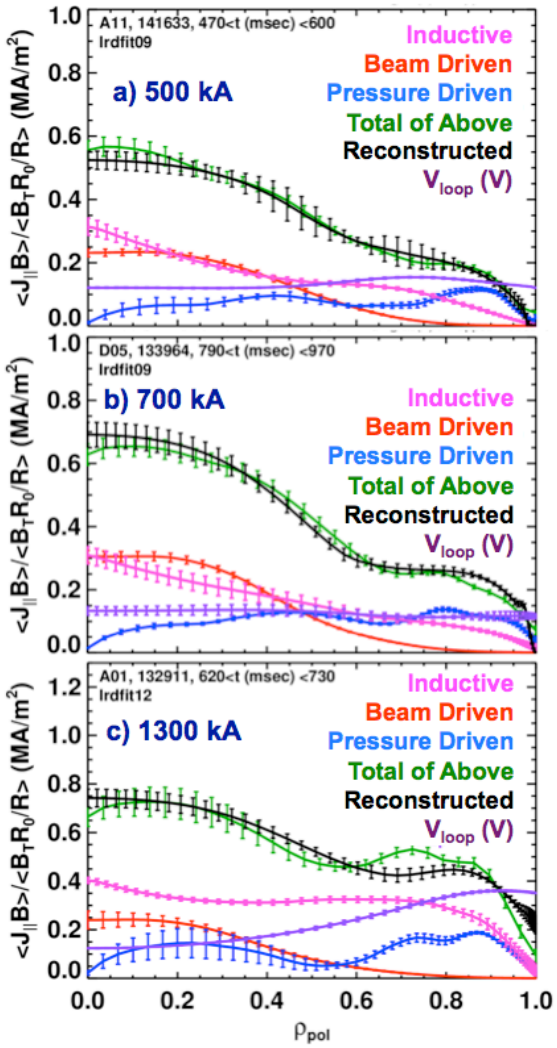

Fig. 7: Analysis of the current profile for a) a low-current discharge designed to maximize β_P (141633), b) a moderate current discharge which has the lowest flat-top average surface voltage of any in NSTX (133964), and c) a high-current discharge designed to maximize the store energy (132911).

5.2: Scaling of the bootstrap fraction with global parameters

Having developed confidence of the applicability of the TRANSP calculations to the analysis of MHD-free periods, we have analyzed the large database of TRANSP runs to look for trends in the bootstrap current fraction. Fig 8a) shows the bootstrap fraction plotted against I_p. For 0.5 MA and above, the bootstrap fraction decreases as I_p is raised, and the general trend is $f_{BS} \propto 1/I_p$. The points at 0.3 MA fall below this trend; these discharges are not typical H-modes, and exhibit weaker edge pedestals (relative to the overall profiles), and less associated bootstrap current, than in the other cases.

Using the standard expression for the bootstrap fraction $f_{BS} = C_{BS}\sqrt{\varepsilon}\beta_{P,th}$, it is found that $C_{BS} = 0.44$ is a good value for this database using the thermal β_P calculated by TRANSP and the Sauter bootstrap model. This expression does not, however, allow a prediction of the bootstrap fraction, as the achievable $\beta_{P,th}$ is determined by transport.

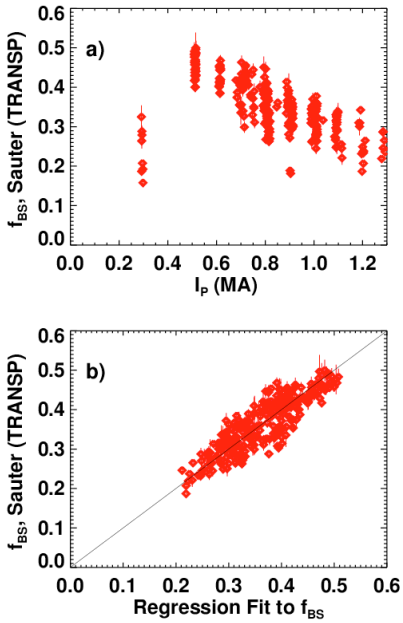

Fig. 8: The bootstrap current fraction plotted against a) the plasma current, b) a regression fit described in the text.

In order to remedy this deficiency, we have applied a regression fit of the form $f_{BS} = CI_P^{\alpha_{I_P}} B_T^{\alpha_{B_T}} n_e^{\alpha_{n_e}} P_L^{\alpha_{P_L}}$ to the TRANSP calculated bootstrap fraction based on the Sauter model. The coefficient C and exponents α were determined using standard multivariate linear regression techniques. We have found that for discharges of the type described in this report, the exponents are generally approximately $-1.05 < \alpha_{I_P} < -0.9$, $0.2 < \alpha_{B_T} \approx 0.3$, $0.35 < \alpha_{n_e} < 0.45$, and $0.15 < \alpha_{P_L} < 0.25$. We can compare these exponents to those expected from transport scaling expressions by noting that $f_{BS} \propto \beta_{P,th} \propto \frac{P\tau_{E,th}}{I_P^2}$. The I_p scaling is consistent, in that $\gamma_{I_P} - 2 \approx -1.1$ is quite similar to the value of α_{I_P}. The fitted B_T and n_e exponents are virtually identical to those from the scaling, and the power scaling of confinement implies $\gamma_{P_L} + 1 \approx 0.25$, also a good match to the bootstrap scaling finding for α_{P_L}. Hence, we find that the bootstrap scaling is consistent with the observed transport scaling in these lithiumized plasmas.

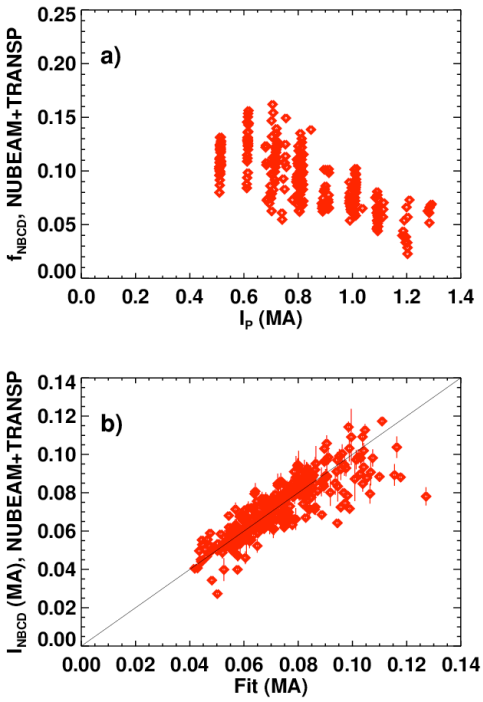

Fig. 9: a) the neutral beam current fraction against I_p, and b) the total beam driven current against the fit described in the text.

5.3: Scaling of the beam current drive with global parameters

The second component of the non-inductive current drive is the neutral beam driven current. The neutral beam current fraction is plotted against the plasma current for the large TRANSP database in Fig 9a). There appears to be a strong $1/I_p$ dependence, though, as will be shown below, this trend is actually a result of the generally higher density at higher plasma current.

We have analyzed this data by fitting it to an expression of the form

$$I_{NBCD} = C_{NBCD}\frac{\overline{T}_e^{3/2}}{\overline{n}_e}\left(P_{inj,A} + 0.85P_{inj,B} + 0.7P_{inj,C}\right). \qquad [1]$$

The ratio $\overline{T}_e^{3/2}/\overline{n}_e$ is a surrogate for the fast-ion slowing-down time and the multipliers on the source B and C powers come from TRANSP runs with individual sources toggled on and off (the bars over T_e and n_e imply that these are line-average quantities). The sources B and C are less efficient in driving current than A because they inject at smaller tangency radius; a larger fraction of their injected ions are born on trapped particles orbits. The powers in the expression are the injected powers, and no accounting is made for the I_p dependent fast-ion loss.

The electron temperature is determined by transport, and we have determined the scaling of the quantity $\overline{T}_e^{3/2}/\overline{n}_e$ by doing regression; the result is $\frac{\overline{T}_e^{3/2}}{n_e} \propto I_P^{1.1} B_T^{0.25} n_e^{-1.6}$ for the NSTX data. Inclusion of P_L in the scaling does not improve the fit in a meaningful

way. This expression is approximately consistent with confinement scaling, using $\overline{T} \propto \frac{P\tau_{th}}{n}$. We have used this regression analysis for $\overline{T}_e^{3/2}/\overline{n}_e$ in Eqn. [1], with $C_{NBCD} = 0.198$. The result is shown in Fig. 9b, where it is clear the fit captures much of the necessary physics. Taking the strongest dependencies, we see that the neutral beam driven current fraction can be expressed approximately as $f_{NBCD} = C_{NBCD} I_P^{0.1} \overline{n}_e^{-1.6} B_T^{0.25} \left(P_{inj,A} + 0.85 P_{inj,B} + 0.7 P_{inj,C} \right)$, which, due to the confinement scaling in NSTX, is largely independent of the plasma current. Hence, the apparent $1/I_p$ dependence in Fig. 9a) is due to the larger density in NSTX when the plasma current is increased.

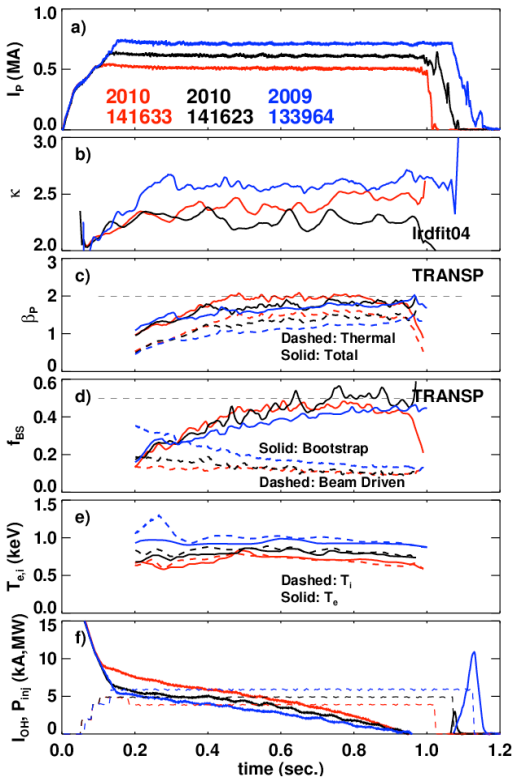

Fig. 10: Time traces for high-β_P discharges. Shown are a) the plasma current, b) the elongation, c) the thermal and total β_P, d) the bootstrap and neutral beam current drive fractions, e) the central electron and ion temperatures, and f) the solenoid current (solid) and injected power (dashed).

5.4 Development of scenarios with very high β_P.

In the process of collecting the lower-current part of this dataset, we developed for the first time in NSTX scenarios with sustained $\beta_P = 2$. An example set of these discharges in shown in Fig. 10, where we consider the 0.7 MA case discussed in Figs. 1, 2c, and 7b), a 0.6 MA case, and the 0.5 MA case shown in Fig. 7a). The injected power (in frame f)) is reduced as I_p is reduced, in order to reduce the loss power at lower current. Indeed, TRANSP shows that the fast ion power lost from charge exchange and bad orbit loss is roughly constant across the scan, as both the power and current are

reduced. The three discharges are also run with different elongations, as shown in frame b). We see that the thermal β_P scales as approximately as $1/I_p$, consistent with the scaling noted above. The low current discharge sustains $\beta_P = 2$, which is the highest in the NSTX database. The bootstrap fraction current for the 0.6 and 0.7 MA cases follow the $0.44\sqrt{\varepsilon}\beta_{P,th}$ rule noted above; the 0.5 MA case, however, falls below this formula, due to changes in the collisionality at reduced T_e and T_i. The neutral beam driven fraction is largest in the high current case, due to the higher beam power and higher temperature which increase the slowing down time. The bottom frame shows the flux consumption, which is on average higher for the lower current cases. TRANSP calculates that the Ohmic current fraction is essentially constant across the scan, such that $I_{OH} \propto I_p$; the increased flux consumption at low I_p is due to the lower electron temperature and higher neoclassical resistivity.

6. Global Stability of High Performance Discharges

The achievable non-inductive fraction is limited by stability as well as confinement. This is fairly obvious in the case of the bootstrap current, whose fraction of the total plasma current scales like $\varepsilon^{1/2}\beta_p \propto q\beta_N$. It is also true for the neutral beam driven current, since this increases with T_e for fixed power; a low β limit may also limit the allowable current drive power. In this section, we discuss the two important performance limiting instability mechanisms during the flat-top if high-β H-mode discharges: global $n = 1$ kink/ballooning stability, and $n = 1$ core kink/tearing. We also discuss the recently implemented β_N control system.

6.1) β_N Control

An important new tool for scenario development in NSTX is the realtime adjustment of the injected power to control the plasma normalized-β, β_N. The normalized β is calculated in realtime with rtEFIT code [70,81]. A PID operator is then applied to the difference between the requested and achieved β_N, to calculate a new input power request which is then translated to pulse-width modulation of the individual beam sources. The technical details of this system are described in Ref. [82].

An example use of this capability is shown in Fig. 11, where the target plasma is a $\kappa = 2.5$ high performance scenario at 0.8 MA. The two black discharges are run with 6 MW of pre-programmed neutral beam power, and are seen to develop RWMs and disrupt at t = 0.8 s. The green and red discharges were run with the β_N control algorithm turned on at t = 0.2 s. The β_N value when the controller is turned on is somewhat greater than the request, and the controller responds by reducing the power (note also that the better-constrained off-line EFIT, shown in frame c), generally produces a higher value of β_N than the realtime value from rtEFIT.) The β_N value is consequently somewhat lower in the red and green cases, and the discharges are sustained for significantly longer. The red case develops a core $n = 1$ mode that eventually locks to the vessel and disrupts, while the green case eventually suffers from an H→L back-transition; neither of these

disruptions appears to result from exceeding the β_N limit. The blue discharge also utilizes β_N control, but with a slightly higher β_N request. There is consequently more power provided to the discharge and a higher β_N value, and the discharge disrupts at nearly the same time as the 6 MW references. This example shows that the β_N controller can indeed improve higher-performance discharges, though a judicious β_N request is required. For instance, the ramp in the request was found to be necessary in this scenario, as having the higher request early invariably lead to disruption. Note that this issue could be eliminated by feeding back on a more accurate estimate of proximity to a stability boundary, for instance, the plasma amplification of an applied $n = 1$ field [83].

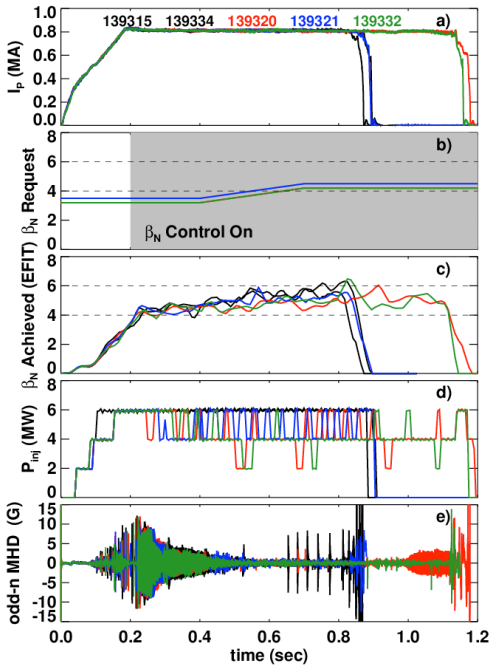

Fig. 11: Demonstration of the newly developed β_N control in NSTX. Shown are a) the plasma current, b) the β_N request, c) the achieved β_N, d) the injected power, and e) the odd-n rotating MHD activity. The time window when β_N control is on is indicated in the gray shading in frame b).

This new capability for β_N control has also been used in support of other experiments. For instance, it was utilized to maintain constant β_N during I_p and B_T scans associated with a tearing mode onset experiment; use of the algorithm to adjust the injected power minimized the number of discharges by eliminating the need to manually adjust the injected power waveform for each I_p and B_T combination [82].

6.2) n=1 Kink/Ballooning Stability

The data presented in Fig. 4 indicate that the plasma shape plays a profound role in determining the high-β performance of the discharge [49]. The profile shapes also play an important role in determining the global stability. Broader pressure profiles improve the plasma global stability [7,84-87]. Reducing the internal inductance tends to be destabilizing (as current accumulates at the edge of the plasma), with instability predicted at very low β_N for sufficiently low l_i [7,84]. We assess these predictions with the database

analysis in Fig. 12. The blue points are from the standard post-shot EFIT~~02~~ at the time of maximum stored energy, while red points are from the database of TRANSP runs described in Sect. 4. These figures update the analysis presented in papers such as [5,31,32,37,41,88] with the most recent data, and with TRANSP data in addition to that from Grad-Shafranov reconstructions.

In Fig. 12, frame a), it is seen that β_N/l_i values of up to 13.5 have been sustained for more than two energy confinement times. In fact, no hard limit on this parameter has yet been observed, with improvements to RWM control system improving the reliability of operation in the low-l_i state [89]. It is interesting to note, however, that l_i values below 0.4 have not been achieved for β_N>~1. This may be an equilibrium limitation given the NSTX current drive sources, though evidence is presented below that NSTX may, at least transiently, be approaching the low-l_i limit. The physics of this regime remains under active investigation [89].

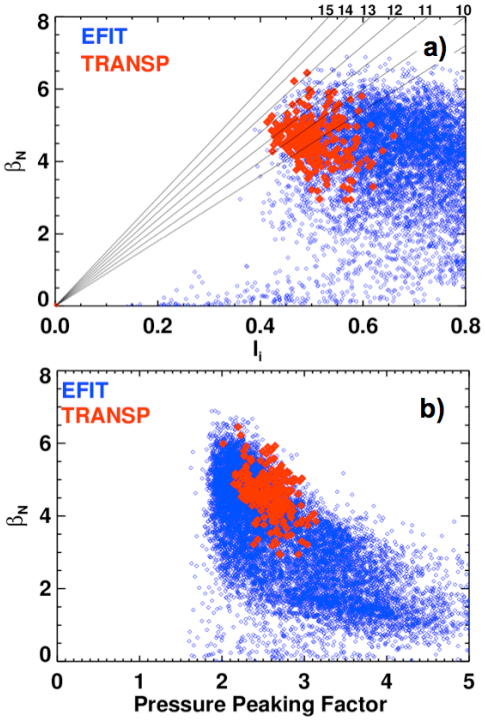

Fig. 12) Plots of the achievable β_N vs a) the internal inductance, and b) the pressure peaking factor. The blue points are from EFIT at the time of maximum stored energy, while the red points are from the database of TRANSP calculations.

A more firm stability boundary has been observed in the space of β_N vs. pressure peaking factor (F_P), defined as the central pressure normalized to the volume average pressure. This is shown in frame b), and we note that TRANSP tends to compute a higher peaking factor that EFIT, due to the explicit inclusion of the peaked fast ion pressure profile; the TRANSP points that sit to the right of the main data mass generally correspond to EFIT points on the left. We find that experimentally, there is an extremely strong dependence of the achievable β_N on the pressure peaking. This reinforces the

importance of achieving H-mode, with broad pressure profiles, for sustained high-β operation [31].

In order to explore the ideal stability physics of these scenarios in more detail, the no-wall and with-wall β_N limits have been calculated as a function of time for a number of high-performance discharges, using techniques described in Sec. 2. A summary of this analysis is shown in Fig. 13, where four discharges are analyzed in detail. The internal inductance and q_0 come from the equilibrium reconstructions that drive the stability calculations, while the β_N and pressure peaking are derived from both the equilibrium reconstructions (solid) and TRANSP (dashed) calculations. We note that, especially early in the discharge, TRANSP predicts a larger pressure peaking than is reconstructed; this is the early phase of the discharge when the fast-ion pressure is proportionally larger. Alfvénic and tearing activity that is common in the early phase of the discharge may result in some radial redistribution of those fast ions. This effect would be captured in the equilibrium reconstruction but not the TRANSP calculation, which assumes classical fast-ion physics.

The four discharges illustrate different trends in these ideal stability metrics. Starting at the upper left and moving counter-clockwise, discharge 134767 is a typical 0.9 MA, $\kappa = 2.3$ H-mode discharge, with somewhat higher l_i and moderate pressure peaking. The resulting no-wall β_N limit of 4.1-4.4 is typical of a large fraction of NSTX discharges.

The next frame shows a 1 MA, $B_T = 0.4$ T, $\kappa = 2.6$ discharge designed to provide the highest possible sustained β_T, and which achieves very high β_N/l_i. There is an early period just before the end of the current ramp, when l_i transiently drops below 0.4. The calculated no-wall β_N limit drops precipitously at this time, but recovers when l_i rises again. This trend has been observed in calculations for many discharges which have $l_i < \sim 0.4$ early in the discharge, and may be indicative of proximity to the low-l_i kink boundary. We note, however, that the current profile is still rapidly evolving during this phase; the development of scenarios with lower-l_i during the more steady phase remains a high-priority research topic. The later phase of this discharge reaches $\beta_N \sim 6$ at $l_i \sim 0.45$, corresponding to $\beta_N/l_i = 12–13$. The pressure peaking factor is reasonably low during this phase of the discharge, and so the no-wall β_N limit stays reasonably high despite the lower internal inductance. The central safety factor continues to evolve in this case, passing through $q_0 = 1$. The final disruption is quite rapid, with a collapse of the edge followed rapidly by the global thermal quench.

The final two figures show the calculation for the 700 kA long pulse and high-β_P discharges discussed above (in Fig. 1, and Figs. 1, 2c, 7b, and 10 respectively). The internal inductance stays low, but the pressure peaking is significantly higher than the 1100 kA case. This combination results in a significantly reduced no-wall limit of ~3.5.

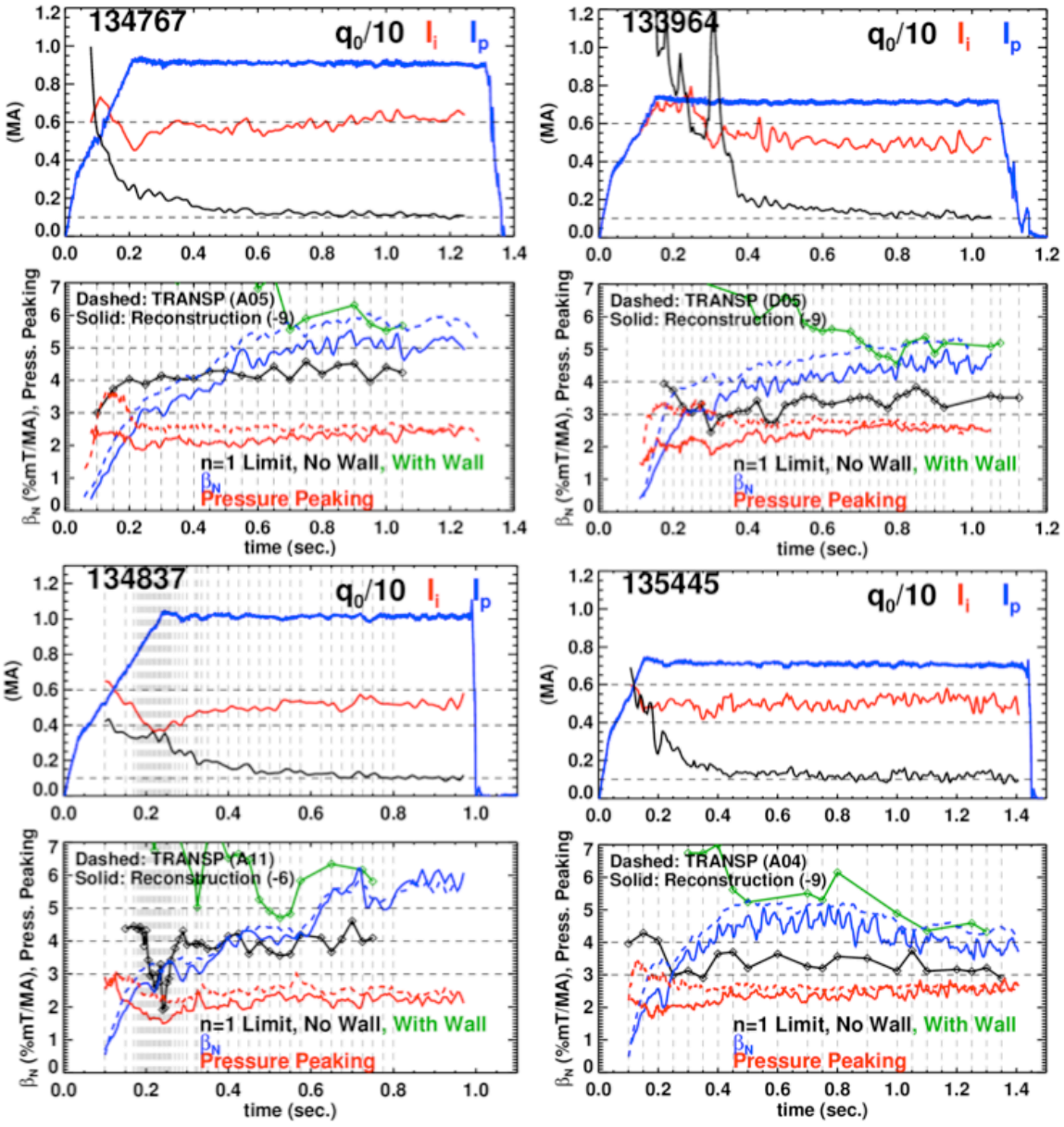

Fig. 13) Calculations of the no- and with- wall ideal MHD stability limits for high-performance discharges. The top figure in each pair shows the plasma current, internal inductance, and central safety factor. The bottom figure shows the normalized β, pressure peaking factor, and no- and with-wall stability limits. The chosen discharges are, going counter-clockwise from the upper left: i) a standard I_P=0.9 MA, κ=2.3 H-mode plasma with higher l_i, ii) a discharge optimized to study sustained high-β_T (1.0 MA and 0.4 T) with a transient low-l_i phase and very high β_N/l_i, iii) a long-pulse scenario (0.7 MA and 0.38 T) with lower-l_i and higher pressure peaking, and iv) a high-β_P (0.7 MA and 0.48 T) scenario with lower-l_i and higher pressure peaking.

The ideal-wall limit in all these cases decreases with time, presumably due to continues evolution of the current profile, and the experimental β_N value becomes comparable to ideal limit at the end of the discharge in all examples. Detailed parametric studies of how these beta limits depend on these profile and shape parameters will be the subject of future scenario research.

While the ideal kink can be stabilized by an appropriately placed superconducting wall, the finite conductivity of the actual wall allows the RWM to grow on the L/R time of the wall eddy currents. As noted in Sec. 2, we stabilize the RWM both passively via plasma rotation, and actively using feedback on the n=1 perturbation using midplane radial field coils [36,39,41,42]. This stabilization is critical to the performance of these discharges, and the reader it referred to Refs. [34,36-39,41,42,90] for additional information.

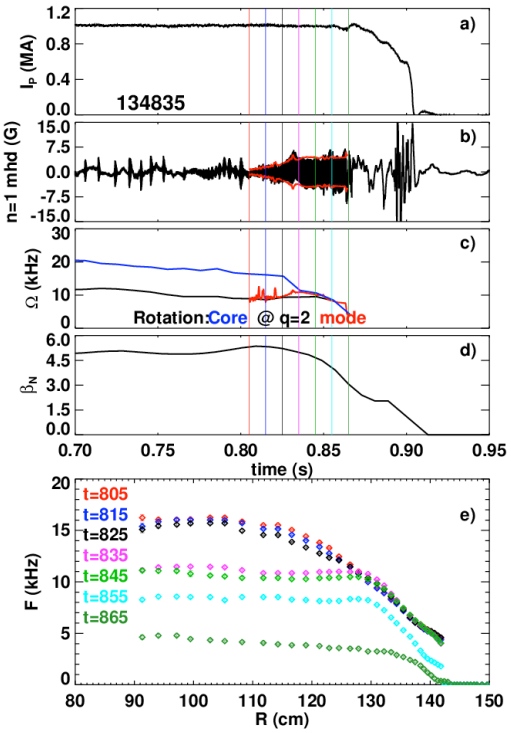

Fig. 14: Effect of a rotating n=1 MHD mode on the global performance. Shown are a) the plasma current, b) the odd-n rotating MHD signature and mode envelope, c) the mode frequency and rotation in both the core and at the q=2 surface, d) β_N and e) the rotation profile evolution at various times.

6.3) Core n=1 Kink/Tearing Modes

In addition to ideal instabilities like the RWM, $n = 1$ core kink/tearing modes have been observed to deleteriously impact performance in these discharges over a wide range of q_{95}. An example of this degradation is shown in Fig. 14, for a $\kappa = 2.5$, $I_p = 1$ MA target. Frame b) shows that an $n = 1$ mode begins to grow at $t \approx 800$ ms, as indicated by the red outline in frame b). The value of β_N at this time is approximately mid-way between the ideal mhd no-wall and with-wall stability limits (of 4 and 6 respectively). The initial frequency of the mode in red in frame c) is an excellent match to the rotation frequency of the $q = 2$ surface, but differs considerable from the core frequency; this implies that the mode will have a strong $m/n = 2/1$ component. There is a rapid collapse

in both the rotation velocity and β_N once the mode reaches large amplitude, indicating the incompatibility of this MHD activity with sustained high-performance operation.

The rotation profile is shown for a few times during the mode growth and saturation in frame e). The profiles are initially somewhat peaked, with central values of ~15 kHz. The rotation collapses when mode strikes, ultimately leading to a configuration with very flat profile inside of the $q = 2$ surface. This is also indicated in frame c), where the core and $q = 2$ rotation are identical once the modes grows large.

The structure of this mode can be better understood using data from the NSTX ultra-soft X-ray (USXR) array [91]. Data from this array is shown in Fig. 15a), where the data have been band-pass filtered, and the tangency radius of the chords is approximately indicated (see Fig. 16 for the geometry of the array). There is a clear inversion in the emission contours across the chord which is approximately tangent to the $q = 2$ surface (chord 10); this is indicative of a magnetic island. There is an additional phase shift across the magnetic axis; this indicated the presence of an odd-n perturbation in the plasma core.

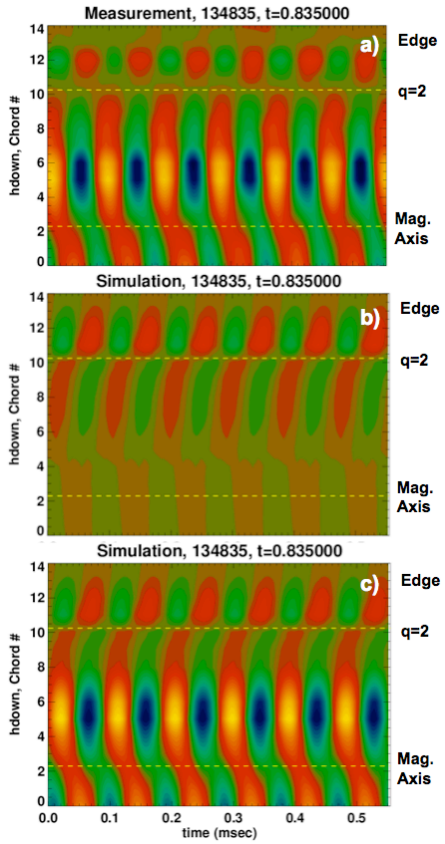

Fig. 15: USXR data for the saturated 2/1+1/1 instability. Shown are a) the chord average measurements, filtered within the frequency band 3<f (kHz)<17, and simulation of the measurement using b) only an m/n=2/1 magnetic island, and c) the model eigenfunction in Fig. 16, with both a 2/1 island and a 1/1 core kink.

A model eigenfunction, described in Ref. [80] and based on the model presented in Ref. [92], has been used to understand the saturated mode structure. This model has both a 2/1 magnetic island, and a $m/n = 1/1$ core kink. The radius of the magnetic island is determined by the radius of the $q = 2$ surface in the underlying reconstruction, while the width of the island is a free parameter. The core kink is modeled as a rigid shift of the magnetic surfaces, with the radius and magnitude of the shift as free parameters. These free parameters are determined by manual adjustment, in order to achieve a good match between the measured and simulated USXR emission contours. We note that this model is not fully physics based, and is used only to provide a qualitative understanding of the mode.

The application of this model to the data is shown in Fig. 15, frames b) and c). If only a $m/n = 2/1$ island is included as in b), the inversion across chord 10 can be reproduced, but not the phase shift across the magnetic axis. When the core kink is added to the 2/1 island in frame c), the simulated and measured emission contours are quite comparable. Note that the color scale of Fig. 15 is arbitrary, but is identical in all frames.

The best-fit eigenfunction for the data in Fig. 15 is shown in Fig. 16. The large 2/1 magnetic island is clearly visible in the red surfaces; the island has an outboard midplane full width of 7 cm, which is approximately consistent with the width of a flat region in T_e observed at that time. The size of the core 1/1 displacement can be seen by comparing the equilibrium surfaces in green to the perturbed surfaces in blue.

We have repeated this analysis for various times in the mode evolution, and found eigenfuctions that are essentially similar to that in Fig. 16. This is true for t=0.825, when there is still significant differential rotation between the $q = 2$ surface and place core, and at $t = 0.86$ s, when the mode has slowed considerably. In general, we find that the core and $q = 2$ perturbations are both present from as early as the present analysis method allows; the perturbations are phase locked from very early time as well. This is consistent with the simulations of a similar instability by Breslau [93]. This large core perturbation also explains the rapid rotation damping. The mode structure is locked to the $q = 2$ rotation frequency, implying that the core plasma must flow through this large 3D magnetic perturbation. The neoclassical toroidal viscosity (NTV) [41,92,94-99] due to this perturbation results in very strong braking of the core flow [92], which is rapidly brought to the level of the perturbation, i.e. the rotation frequency of the $q = 2$ surface.

This discharge eventually suffers a H→L back-transition at $t = 0.8636$ s after the bottom plasma-wall gap transiently goes to zero. However, as is shown in Fig. 17, the mode structure is preserved across the transition. Both the core kink, and the 2/1 island inversion radius, are still present. This structure makes approximately 10 revolutions before finally locking to the wall.

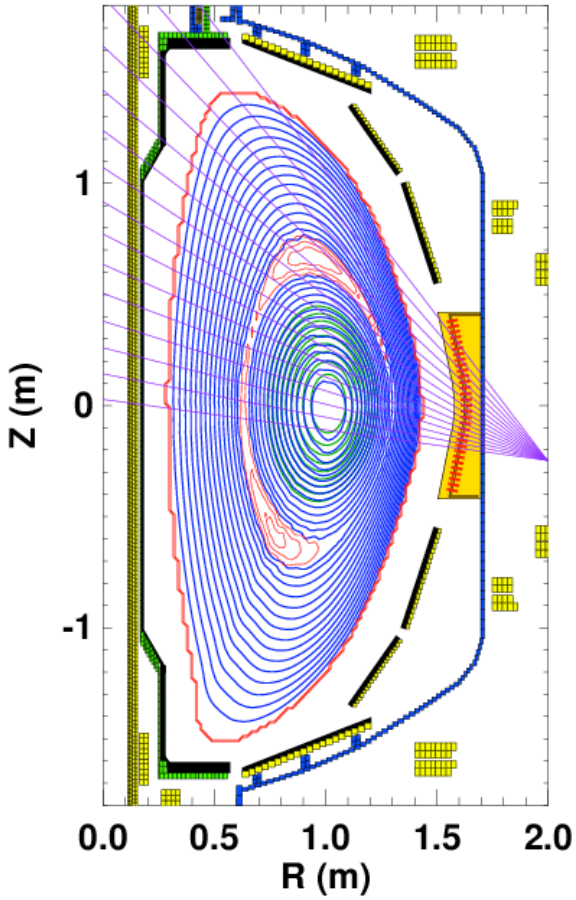

Fig. 16: Model eigenfunction for the simulations in Fig. 15. The closed (perturbed) magnetic surfaces are shown in blue, while the island contours are in red. The unperturbed core surfaces are shown in green. Also shown are the chords of the USXR detector.

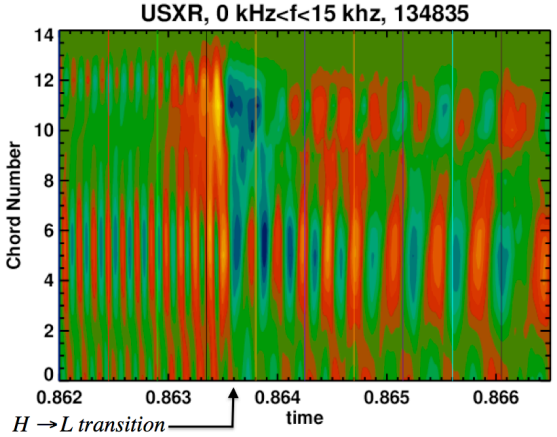

Fig. 17: Evolution of the USXR emission across the H->L back transition at 0.8635. The rotation frequency is much lower after the back transition, but the structure is similar.

These coupled-modes instabilities are quite common in long-pulse NSTX plasmas. For instance, Ref. [80] shows a very similar eigenfunction, for a 0.7 MA, 0.48 T

discharge targeting high-β_P. Evidence is presented there that these modes can lead to substantial modifications to the bean driven current profile, complementing studies in Ref. [35] where the impact of single 1/1 mode on the current profile was studied. They can be triggered by ELMs, EPMs, or grow from vanishingly small amplitude [100]. Many of the dynamics of these modes can be understood in terms of neoclassical island physics; the modes are often triggered, and power ramp experiments have shown an $n = 1$ magnetic perturbation amplitude proportional to β_P^2, as expected for an NTM [101]. However, this paradigm fails to account for the 1/1 component, which can be ideally unstable [93], and may account for the observed mode onset in the absence of an observable trigger. The ideal stability is quite sensitive to the increment of the safety factor above unity [93,102], and underscores the importance of maintaining an elevated q_{min}.

We also note that "long-lived" 1/1 modes have been observed in MAST beam heated discharges [102]. These modes are similar to those discussed here, in that they have a strong $m/n = 1/1$ core kink component, contribute to strong rotation braking and confinement degradation, and lead to fast ion redistribution. They differ, however, in that the modes in MAST do not show any tearing at the $q = 2$ surface, and always rotate with the frequency of the core plasma. The modes in NSTX do show tearing, and, from the earliest possible time in the mode evolution, rotate with the frequency of the $q = 2$ surface.

7. Proximity to steady state

Given the results presented in the previous section, it is interesting to ask what increment of performance improvement would be required to achieve steady state. We have approached this exercise by taking discharge 133964, illustrated in Figs. 1, 2c, 7b, 10, and 13, and scaling the electron and ion temperature profiles (the two profiles are scaled by the same amount, so that their ratio is the same as the underlying experimental case). The Z_{eff} profile was fixed flat at 3, while the electron density profile was set to that in the experiment. The field, current, and heating systems in these simulations were the same as in the actual experiment. The calculations were done with TRANSP solving the poloidal field diffusion equation, and were run sufficient long that the current profile stopped evolving, i.e. the loop voltage profile became flat and the q-profile became stationary. This occurred over ~400 msec for the base case, and ~700 msec for the case below with largest temperature multiplier. We note that these simulations are not fully self-consistent, in that the thermal profiles were not permitted to evolve as the current profile changed, despite the known dependence of transport on the current profile shape [103-106].

The results are shown in Fig. 18. Frame a) shows various quantities as a function of the assumed temperature profile multiplier. Most importantly, the non-inductive fraction reaches 1 with a simple temperature multiplier of 1.4. This corresponds to achieving a confinement enhancement of 1.5 with respect to ITER-98 scaling, and an increase in β_N from 4.7 to ~6.5 (no stability assessment has been made on these

equilibria). The central safety factor is raised from 1 to 1.45, which would be quite useful for avoiding the core $n = 1$ modes described in section 6; the mid-radius collisionality υ_e^* is reduced by ~50% over this scan, from 0.17 to 0.09.

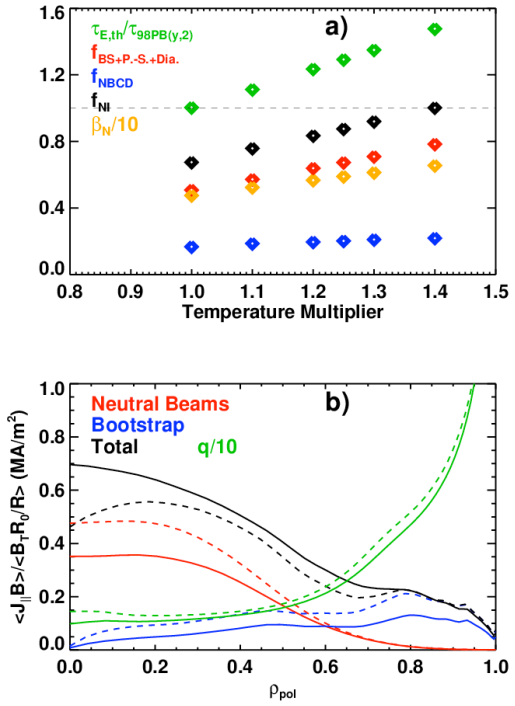

Fig. 18: Dependence of the confinement time, pressure-driven current fraction, beam current drive fraction, total non-inductive fraction, and β_N on the temperature multiplier in the TRANSP simulations, and b) profiles for the base configuration (solid), and fully non-inductive configuration (dashed).

The current and safety factor profiles for the base (solid) and fully non-inductive (dashed) cases are shown in frame b). There is an increase in bootstrap current across the profile, as expected when the temperature increases. The bootstrap fraction actually increases faster than the thermal β_P, as a result of the decreasing collisionality. The beam current drive increases, due to the longer slowing down time. This increase in central driven current does not, however, lead to a reduction in the central safety factor, as the otherwise centrally peaked Ohmic current is eliminated in this fully non-inductive case.

Other modifications to the profiles to achieve $f_{NI} = 1$ are possible. For instance, if Z_{eff} is reduced to 2, then the required temperature multiplier for non-inductive operation is reduced to 1.3. The example given above is sufficient to demonstrate that the present NSTX discharges are approaching a fully non-inductive state. We note the recent development of the "enhanced pedestal" H-mode [107] provides a scenario with confinement multipliers of the size noted above, though this scenario has never been sustained in this high-elongation, high-q_{95} scenario.

8: Development of Advanced Divertors

A critical issue for future ST (and larger aspect ratio tokamak) development is the handling of large heat fluxes in the divertor; material properties and active cooling technology limit steady state heat fluxes to ~10 MW/m^2 on the divertor material surface [108]. The plasmas described above have two features that can serve to mitigate the otherwise large heat fluxes. First, they are all very near double-null; i.e. the separatrices defined by the primary and secondary X-point are almost degenerate at the midplane. This has been shown to reduce the heat flux at the divertor plate by dividing the power between the upper and lower divertors [46]. Secondly, the high elongation results in the X-point being close to the divertor floor, which increases the flux expansion and has been shown to reduce the peak heat flux [109].

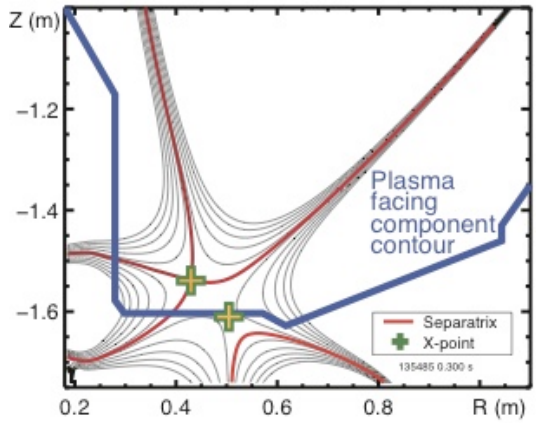

Fig. 19: Magnetic geometry of a snowflake divertor in NSTX.

Although desirable, these features alone may not be sufficient to reduce the heat flux to the required level in a next step device (the heat fluxes in the present NSTX discharges are acceptable). Hence, we have developed configurations with a "snowflake" divertor [55,110,111]. A standard tokamak divertor is formed by creating a first order magnetic field null between the plasma current channel and a single divertor coil. In a snowflake divertor [112,113], a second order field null is created through the use of a second divertor coil: the divertor coil currents are adjusted so that the X-points formed between the plasma current channel and the two coils are close or overlapping. When they overlap, both the magnitude and gradient of the poloidal field vanish at the X-point. This results in a divertor configuration with larger flux expansion and longer field line connection length.

An example equilibrium of an experimentally achieved snowflake divertor is shown in Fig. 19. The region of expanded poloidal flux in the vicinity of the two X-points is clearly visible. Note that this configuration was produced with only two divertor coils.

Many of the postulated benefits of the snowflake divertor configuration have been confirmed in NSTX [111]. Discharges with a snowflake divertor exhibited beneficial impurity screening, with a substantial reduction in core carbon, without deleterious effects on the core plasma configuration. Detailed analysis showed that the outer strike point was detaching in these configurations, despite the lithium PFC conditioning which tends to inhibit detachment by reducing recycling and the divertor electron density.

Increases in divertor radiation and volumetric recombination, both signs of detachment, were observed, and the peak heat flux dropped precipitously. It appears likely that the reduced divertor temperature in these configurations resulted in reduced rates of physical and chemical sputtering. The reader is referred to Refs. [55,110,111] for further information.

9. Extension to higher aspect ratio

The results in the previous sections were from plasmas where the aspect ratio was deliberately maintained at a low value. Many next-step ST designs, however, call for operating at somewhat higher aspect ratio, while maintaining high-elongation. This is motivated by the need to increase the size of the TF bundle to reduce the Ohmic dissipation, since copper, not a superconductor, is typically used to manufacture this coil [11,13]. As shown by the black labeled points in Fig. 20, these include the proposed NSTX-Upgrade [114], a recent "Pilot Plant" study [11], and some designs for a fusion nuclear science facility [13]. The increasing aspect ratio is generally deleterious to the n = 0 (vertical) and n = 1 (kink/ballooning) stability of the plasma. Hence, we have conducted an initial experiment to assess the performance of higher-aspect ratio plasmas in NSTX, and to determine how the previously presented results scale to this class of next-step design. We note that the machine conditions were not optimal when these discharges were run.

Example shapes at the limits of this study are shown in Fig. 21. Discharge 142305 has $\kappa = 2.45$, $A = 1.45$, and is typical of high-performance plasmas discussed above. Discharge 142301 is a $\kappa = 2.9$, $A = 1.7$. The primary means of increasing the aspect ratio was to increase the PF-1A coil current, as this increases the inboard midplane plasma-wall gap. The outboard midplane plasma wall gap was fixed to ensure that all discharges in the scan had similar coupling to the outboard stabilizing plates; a large value of ~16 cm was used to avoid fast ions interacting with structures on the outboard midplane. Note that these elongations are comparable to the highest ever in NSTX [46], but at higher aspect ratio; they are also sustained for considerably longer. Finally, we note that the inner-wall and divertor outline for NSTX-Upgrade are indicated in the magenta line. Discharge 142301 would easily fit in that outline, and this shape can be regarded as near proto-typical for high-performance plasmas in NSTX-Upgrade (the divertor coils for NSTX-Upgrade will have larger radii than at present, and so will eliminate the near-contact of the plasma boundary with the inner wall apparent near the X-points.).

Figure 20 shows the expanded aspect-ratio vs. elongation space for NSTX. The black lines indicated the standard operating space of NSTX, with the blue points coming from the previously discussed database of high performance discharges. All previous scenario development work in NSTX fit within the line shown in gray. The discharges from the present experiment are indicated by the line of red points. There is a clear relationship between the elongation and aspect ratio. If the inner gap is made larger at fixed plasma height and outer gap by increasing the divertor coil current, the elongation increases. If the elongation is made larger at fixed divertor coil current and outer gap by

reducing the pushing field from the PF-3 coils, the inner gap becomes larger, increasing the aspect ratio. Note that NSTX, and most STs in general, do not have shaping coils on the inboard midplane, so that the inner gap typically changes along with other shape parameters.

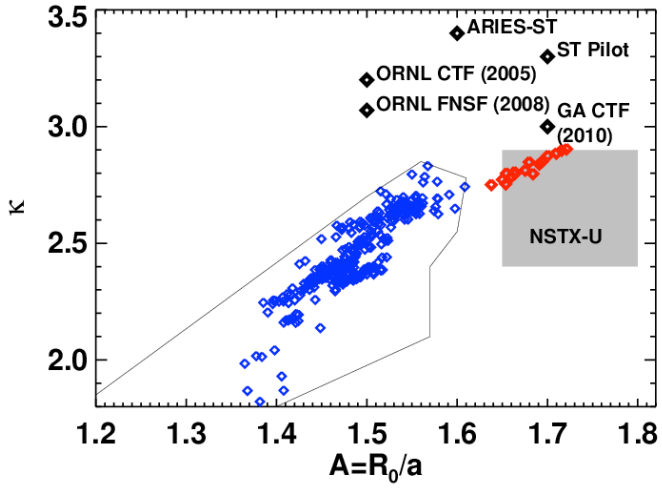

Fig. 20. Space of elongation vs. aspect ratio for NSTX discharges. The black line encloses the historical NSTX operating space for discharges with flat-top duration exceeding 0.5 s, and specific high-performance discharges are indicated in blue. The points collected in the high aspect-ratio experiment are indicated in red. The approximate NSTX-Upgrade [114] operating space is indicated in a gray box, and the parameters of a few next-step ST designs, corresponding to Refs. [8,9,11,13 & 15], are indicated with black diamonds.

The time history of example discharges in this scan are shown in Fig. 22. All discharges have $I_p = 0.9$ MA and $B_T = 0.45$ T. The discharges have the same startup, with the aspect ratio and elongation ramping up after I_P reached flat-top. All discharges in this scan are initially heated with 5 MW of power, dropping to 4 MW at 0.6 s. All discharges achieve $\beta_N \geq 4$, though there is a clear drop in β_N for the higher aspect ratio cases. Note that for fixed current, field, and injected power, β_N is proportional to the confinement time divided by the plasma height. We observe a small reduction in confinement for the larger aspect ratio, while the plasma overall height is increasing in the scan; these trends account for the drop in β_N. The internal inductance is kept quite low in this scan (and decrease with increasing A and κ), and the highest aspect ratio point sustains $\beta_N/l_i > 8.5$.

It was noted above that the calculated $n = 1$ ideal stability would degrade when the aspect ratio and elongation were increased. This is demonstrated in Fig. 23. The blue points are the achieved values of β_N for time-slices in the window $0.5 < t < 0.7$ s. The red points are the $n = 1$ no-wall limit, calculated using the same methods as described in Sects. 2 & 6; note that these calculations are based on reconstructed equilibria, and so include the effects of any pressure and current profile variation as the aspect ratio is changed. The red line shows a simple fit to the data to guide the eye. The values of elongation (κ), q_0, pressure peaking (F_P), and internal inductance (l_i) are shown in the bottom frame. As discussed above, there is an upward drift in elongation as the aspect ratio is increased; there is also a small but monotonic drop in the internal inductance. The

time slices where chose such that F_P and q_0 were kept within the bounds $2.15 < F_P < 2.4$ and $1.1 < q_0 < 1.4$. We did not see clear trend in pressure peaking with increasing A, while all discharges evolved toward $q_0 = 1$.

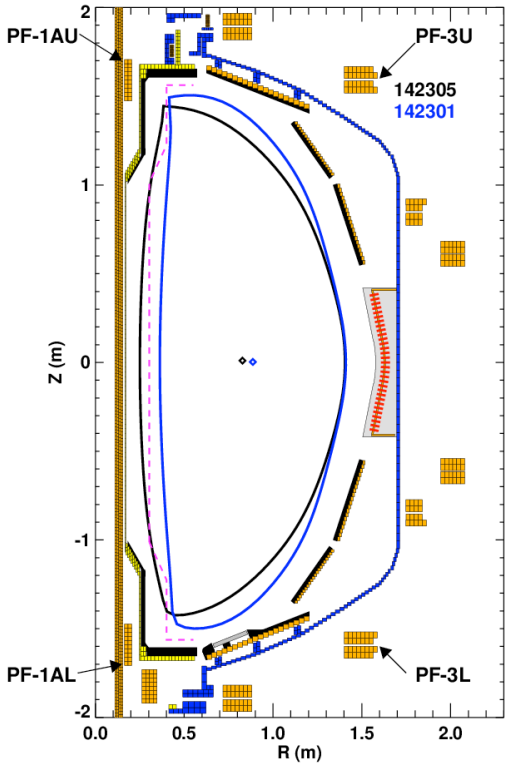

Fig. 21: Plasma boundaries for a typical high-elongation discharge (142305), and a high aspect ratio and elongation discharge (142301). Also shown in magenta is the inboard side PFC boundary for NSTX-Upgrade [114].

The calculated no-wall limit is observed to degrade significantly as the aspect ratio and elongation are increased, dropping by nearly a full unit (%·m·T/MA) in β_N compared to the value ~4.3, which, as noted above, is typical of higher elongation discharges to date. The achieved β_N in blue is roughly constant across the scan. For lower A, the achieved β_N is these discharges is at or beneath the no-wall limit; the higher aspect ratio discharges have β_N above this limit, and are thus potentially unstable to the RWM. Note that no effort was made to test the experimental β_N limit in these scans; the actual experimental β_N limit could be substantially above these blue points (which were achieved with 4 MW of input power). This limit will be tested in future experiments. Also shown in cyan is the no-wall limit scaling from Ref. [5]; the different shape and profile assumptions for that modeling study led to a different numerical value for the β_N limit, but the scaling with A is virtually identical to the calculations based on the achieved profiles.

All discharges in the series in Fig. 22 ultimately succumb to the coupled m/n = 1/1+2/1 kink tearing modes described in Sec. 6; the time of mode onset can be seen as the time when β_N begins to roll over in Fig. 22c). The inversion layer across the

magnetic axis and the $q = 2$ surface is visible in all these cases, and strong rotation damping is observed. The modes in these discharges were not triggered by ELMs or energetic particle modes (EPMs). This further underscores the need to maintain an elevated q_{min} value to avoid these instabilities.

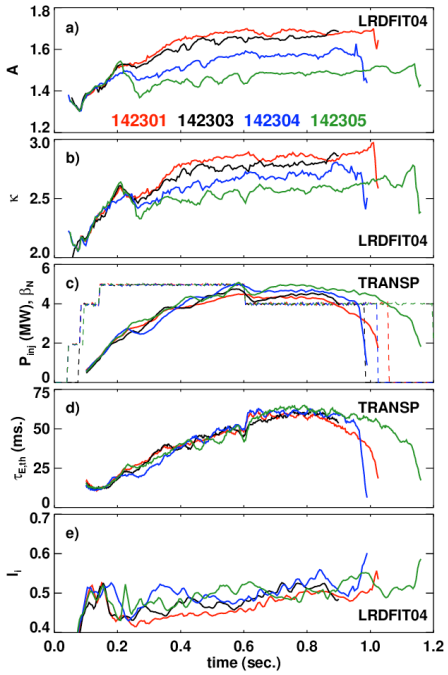

Fig. 22. Time traces from 4 discharges in the aspect-ratio scan. Shown are a) the aspect ratio, b) the elongation, c) the injected power and stored energy, e) the confinement time, and f) the internal inductance.

The natural elongation of the configuration will also be reduced when the aspect ratio is increased [2, 3]. Hence, we have also made an initial assessment of the vertical stability degradation at higher aspect ratio. These experiments were done by freezing the voltage on the radial field coils (PF-3 coils, see Fig. 21) and allowing the plasma to drift vertically; the magnetic axis position was then fit to functions of the form $\delta Z \cdot e^{\gamma(t-t_0)}$. We have observed that the growth rate increases from ~50 s^{-1} at $A = 1.45$ to ~150 s^{-1} at $A = 1.65$, and efforts to model this modification to the vertical stability are underway.

These results do not yet provide a clear positive or negative statement about the physics-side consequences of somewhat higher aspect ratio for next-step STs. The increased vertical growth rate can be countered with improved vertical control systems, and development efforts in this area are ongoing. The reduction in confinement will be revisited with better machine conditions in upcoming campaigns. Most importantly, experiments to probe to ideal MHD & RMW stability limits at higher aspect ratio will be performed, in order to determine the reduction in the actual β_N limit (as opposed to that calculated using ideal MHD).

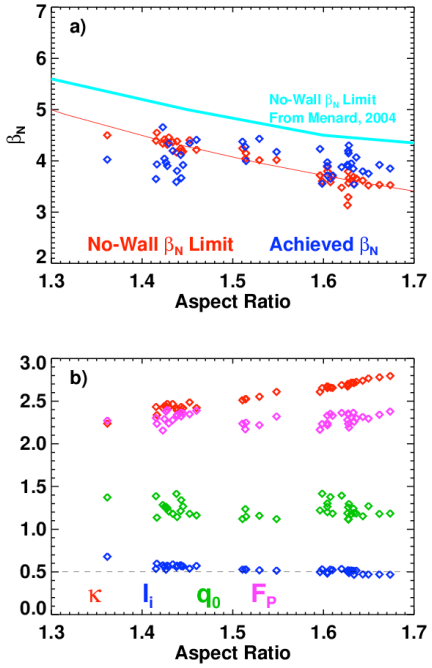

Fig. 23. a) The no-wall β_N limit and achieved β_N, as a function of aspect ratio, and b) the elongation (κ), internal inductance (l_i), central safety factor (q_0), and pressure peaking factor (F_P), as a function of aspect ratio.

10. Summary and Discussion

This paper has described a number of important advances in scenario development in NSTX over the past few years. Important performance figures of merit, all of which are NSTX records in some combination of parameters, include:

- development of a discharge with ~460 kJ of stored energy (Sect. 3),
- development of scenarios with sustained $\beta_P = 2$ and $\beta_T = 20$-25% (Sects. 3, 4, & 5),
- development of H-mode scenarios with surface voltages of ~130 mV (Sects. 3 & 4),
- development of scenarios with sustained $\beta_N/l_i = 11 - 13$ (Sect. 6),
- development and sustainment of high-β, $\kappa = 2.9$ scenarios, at higher aspect ratio ($A \approx 1.67$) prototypical of the proposed NSTX Upgrade (Sect. 9),

Similarly, significant physics progress toward the development of an advanced ST operation point has been made, including:

- development of advanced divertors (Sect. 8),
- demonstration of a modification to the ST H-mode confinement scaling in lithium conditioned high-performance discharges (Sect. 4),
- documentation of coupled 2/1+1/1 instabilities that limit many high-performance discharges when q_{min} approaches 1 (Sect. 6),

- improved benchmarking of current drive calculations against measurements in various discharge regimes (Sect. 5),
- routine operation at lower values of internal inductance than previously possible (Sect. 3).

Given this progress, it is interesting to compare the *core* plasma performance achieved to date in NSTX to that anticipated for next-step devices. Table 1 shows the proposed parameters for NSTX upgrade and four configurations that have been proposed for the study of fusion nuclear science (FNS) [9,13] or nuclear component testing [8,12]. Table 2 shows some parameters for devices designed to generate net electricity, either as a "Pilot Plant" or a full power reactor. These tables include information derived from various published studies, with only trivial calculations used to fill in parameters not directly quoted in the papers. Because not all parameters are given for each study, some elements in the tables are not filled.

Inspection of the tables shows that some common features among the designs, as well as some differences. There is a moderate range of aspect ratios, with more recent studies often using higher values. High elongation is assumed in all cases in order to maximize the bootstrap current. Furthermore, the confinement is typically assumed to exceed the expectations from the ITER98$_{y,2}$ scaling expression, sometimes by a large margin. The power-plant like configurations in Table 2 typically operate at higher β_N, and lower q^*, than the FNS and component test facility (CTF) like configurations.

	NSTX	NSTX Upgrade [114]	FNS/CTF [13]	CTF [8], W_L=2 MW/m^2	CTF [19]	FNS/CTF [9] W_L=1 MW/m^2
β_N (%·m·T/MA)	5-6	5-6	5.2	4.9	3.5	3.8
β_T (%)	15-25	10-25	26	30	17	18
I_p (MA)	0.7-1.3	1.0-2.0	8.4	12.3	6.5	8.2
B_T (T)	0.35-0.5	1.0	2.8	2.5	2.5	2.2
$f_{BS+PD+Diam}$ (%)	40-60	60–80	>75	>60		~50
f_{NB} (%)	5-15	20–40				~50
κ	2.3-2.8	2.6-2.9	3.0†	3.2	2.4	3.1
R_0 (m)	0.85	0.9	1.	1.2	0.85	1.2
A	1.4-1.55	1.65-1.85	1.7	1.5	1.55	1.5
H_{98}	0.9-1.2	0.9-1.3	1.6	2.1	1.3	1.5
q^*	2.5-4.5	3.5-5	3.8	3.1	2.3	3.7
P_{aux} (MW)	3-6	10-18	42	29	44	31

Table 1: Parameters for typical high-performance, lower aspect ratio discharges in NSTX, and proposed parameters for NSTX-Upgrade and four devices designed to do nuclear component testing. († at 95% limit).

	Pilot Plant [11]	Reactor [15]	Reactor [14]	Reactor [16]
β_N (%·m·T/MA)	5.2-6	7.4	8.2	8.2
β_T (%)	30-39	50	59	58
I_p (MA)	18-20	29	31	31
B_T (T)	2.4	2.1	1.8	1.8
$f_{BS+PD+Diam}$ (%)	85-89	96	88	92
f_{NB} (%)	11-15	4	12	8
κ	3.3	3.4†	3.0	3.2
R_0 (m)	2.2	3.2	3.4	3.42
A	1.7	1.6	1.4	1.4
H_{98}	1.3-1.35		1.4	1.6
q^*	2.8-3.0	2.8	2.6	2.8
P_{aux} (MW)	50-60	28	50	50-60

Table 2: Proposed parameters for three ST devices designed to generate net electricity († at 95% limit).

Considering first the plasma shapes, the maximum elongation achieved in NSTX is ~2.9, at aspect ratio $A = 1.7$; this aspect ratio is comparable to (or larger than) that assumed for next-step devices. The elongation, however, is less than that assumed for those devices so a further increase is required. This will result in reduced stability margins for $n = 0$ and $n = 1$ modes, and is a high-priority topic for further exploration.

The presently achieved values of β_N are consistent with the needs of next-step devices for nuclear component testing, though they fall significantly beneath the values assumed in reactor studies. Some uncertainty remains, however, extrapolating the NSTX results to the future because the next-step devices assume operation at lower internal inductance, and higher aspect ratio, than typical NSTX plasmas. These have the effect of lowering the no-wall β_N limit [5,7,84]. Further, the pressure peaking, which is determined by the as yet unknown transport, will have a major impact on the global stability. Furthermore, the rotation and collisionality profiles [34,37,38,115,116] will impact the RWM stability. Hence, while the achievement of long-pulse discharges at $\beta_N = 5 – 6$ is encouraging, the extrapolation to next-step devices requires additional understanding.

With regard to confinement, these devices typically assume confinement that is close to or exceeds the best commonly achieved in NSTX. Figure 5 shows that our sustained high-performance H-mode plasmas generally have $H_{98} \sim 1$, with some best cases [35] achieving $H_{98} = 1.15$; this is at the bottom of the range assumed for next-step devices. While ion thermal transport is generally at the neoclassical level in NSTX H-mode plasmas, the electron transport remains anomalously high. Candidate mechanisms to explain the large transport levels include electron temperature gradient (ETG) modes [117,118], micro-tearing modes [119,120,121], or electron transport driven by energetic

particle MHD [122]. Distinguishing between these various transport mechanisms, and establishing how the transport extrapolates to higher-fields and currents at reduced collisionality, continues to be the subject of intense research in NSTX. We also note that a regime with significantly improved H-mode confinement, known as the "Enhanced Pedestal H-mode" [107] has been produced in NSTX, and efforts to develop it into a standard operational scenario are ongoing.

The most significant gap between the present and next-step device, however, may be with respect to the current drive and the steady-state q-profile. Significantly, NSTX discharges have now routinely achieved pressure-drive current fractions of 50-55%, which is quite close to the requirements for component testing facilities. The present NSTX neutral beam geometry, however, limits their ability to drive current: the sources inject with tangency radii such that the beam current drive efficiency is comparatively low, and the current that is driven tends to reduce q_0 and q_{min}. This central current drive, coupled to the centrally peaked inductive current, tends to drive the onset of performance limiting core $n = 1$ modes at the q_0 drops, as discussed in Sec. 5. The component testing devices in Table 1 rely on significant off-axis neutral beam current drive in order to maintain full non-inductive operation with elevated q_{min}. Fast particle driven MHD can drive significant fast ion loss, as has been observed in NSTX [123,124,125]. These modes can also severely modify the fast-ion driven currents [80,126,127], impacting the current drive assumptions in next-step device designs. The study of fast-ion driven MHD, and its effect on the confinement of those fast ions, is a major object of study at NSTX.

11: Acknowledgements

The authors would like to thank the members of the neutral beam operations team for their help with the β_N feedback system, and the NSTX engineering and operations teams for their support. This research was funded by the United States Department of Energy under contract DE-AC02-09CH11466.

References:

[1] Y.K.M. Peng and D.J. Strickler, Nuclear Fusion **26** (1986) 769.

[2] M. Roberto, Nuclear Fusion **32**, 1666 (1992).

[3] J. E. Menard, et al., Nuclear Fusion **37**, 595 (1997).

[4] R.L. Miller, et al., Physics of Plasmas **4**, 1062 (1997).

[5] J.E. Menard, et al., Phys. Plasmas **11**, 639 (2004).

[6] F. Troyon, et al., Plasma Phys. Control. Fusion **26**, 209 (1984).

[7] E.J. Strait, Phys. Plasmas **1**, 1415 (1994).

[8] Y-K M Peng, et al., Plasma Phys. Control. Fusion **47** (2005) B263.

[9] Y-K M Peng, et al., *Effects of Physics Conservatism and Aspect Ratio on Remote Handling for Compact Component Test Facilities (CTFs)*, Paper FT/P3-14, Geneva (2008).

[10] Y-K M Peng, et al, Fusion Science and Technology **56**, 957 (2009)

[11] J.E. Menard, et al, *Prospects for pilot plants based on the tokamak, ST, and stellarator*, IAEA Fusion Energy Conference, Paper FT/P2-2, Daejeon (2010).

[12] M. Abdou, Fusion Eng. And Design **27**, 111 (1995).

[13] R.D. Stambaugh, et al., *Candidates for a Fusion Nuclear Science Facility (FDF and ST-CTF),* Paper P2.110, 37th EPS Conference on Plasma Physics, Dublin, Ireland (2010).

[14] R.J. Akers, et al., Nuclear Fusion **40**, 1223 (2000).

[15] F. Najmabadi and the ARIES Team, Fusion Eng. And Design **65**, 143 (2003).

[16] H.R. Wilson, et al., Nuclear Fusion **44** (2004) 917.

[17] R.J. Goldston, et al., *An Experiment to Tame the Plasma Material Interface*, IAEA Fusion Energy Conference, Paper FT/P3-12, Geneva (2008).

[18] H.R Wilson, et al., *A Steady State Spherical Tokamak for Components Testing*, IAEA Fusion Energy Conference, Paper FT/3-1Ra, Villamoura, Portugal (2004).

[19] G.M. Voss, et al., Fusion Eng. and Design **83**, 1648 (2008).

[20] A. Sykes, et al., Nuclear Fusion **32**, 694 (1992).

[21] M. Gryaznevich, et al., Phys. Rev. Lett. **80**, 3972 (1998)

[22] D. A. Gates, et al., Phys. Plasmas **5**, 1775 (1998).

[23] M. Ono, et al., Nuclear Fusion **40**, 557 (2000).

[24] A. Sykes et al., Nuclear Fusion **41**, 11 (2001).

[25] R. Maingi, et al., Phys. Rev. Lett. **88**, 035003 (2002).

[26] R. J. Akers, et al., Phys. Rev. Lett. **88**, 035002 (2002).

[27] S.M. Kaye, et al., Phys. Rev. Lett. **98**, 175002 (2007).

[28] S.M. Kaye, et al., Nuclear Fusion **46**, 848 (2006).

[29] M. Valovic, et al., Nuclear Fusion **49**, 075016 (2009).

[30] D. A. Gates, et al., Nuclear Fusion **10**, 1659 (2003).

[31] J.E. Menard, et al., Nuclear Fusion **43**, 330(2003).

[32] S.A. Sabbagh, et al., Phys. Plasmas **9**, 2085 (2002).

[33] R. J. Buttery, et al., Nuclear Fusion **44**, 1027 (2004).

[34] A.C. Sontag, et al., Phys. Plasmas **12**, 056112 (2005).

[35] J.E. Menard, et al., Phys. Rev. Lett **97**, 095002 (2006).

[36] S.A. Sabbagh, et al., Phys. Rev. Lett. 97, 045004 (2006).

[37] S.A. Sabbagh, et al., Nuclear Fusion **46**, 635 (2006).

[38] A.C. Sontag, et al., Nuclear Fusion **47**, 1005 (2007).

[39] J.E. Menard, et al., Nuclear Fusion **50**, 045008 (2010).

[40] S.P. Gerhardt, et al., Plasma Phys. Control Fusion **52**, 104003 (2010).

[41] S.A Sabbagh, et al., Nuclear Fusion **50** (2010) 025020.

[42] S.A. Sabbagh, et al., *Resistive Wall Mode Stabilization and Plasma Rotation Damping Considerations for Maintaining High Beta Plasma Discharges in NSTX*, Paper EXS/5-5, Daejeon (2010).

[43] S.P. Gerhardt, et al., *Development of High-Elongation, High-Beta Discharges for Steady State Spherical Torus Applications*, 37th European Physical Society Conference on Plasma Physics, Dublin, Ireland, online:

http://ocs.ciemat.es/EPS2010PAP/pdf/O5.126.pdf

[44] S.P. Gerhardt, et al., *Progress in the Development of Advanced Spherical Torus Operating Scenarios in NSTX*, Paper EXS/P2-08, Daejeon, South Korea (2010).

[45] D.A. Gates, et al., Nuclear Fusion **46**, S22 (2006).

[46] D. A. Gates, et al., Nuclear Fusion **47**, 1376 (2007).

[47] D. Gates, et al., Fusion Engineering and Design **81**, 1911 (2006).

[48] D. Mastrovito, et al., Fusion Engineering and Design **85**, 447 (2010).

[49] D. A. Gates, et al, Phys. Plasmas **13**, 056122 (2006).

[50] H. Kugel, et al., Phys. Plasmas **15**, 056118 (2008).

[51] M. G. Bell et al., Plasma Phys Control Fusion **51**, 124054 (2009).

[52] R. Maingi, et al., Nuclear Fusion **50**, 064010 (2010).

[53] S.M. Kaye, et al., *L-H Threshold Studies in NSTX*, Paper EXC/2-3Rb, Daejeon, South Korea (2010).

[54] R. Maingi, et al., Phys. Rev. Lett. **103**, 075001 (2009).

[55] V.A. Soukhanovskii, et al, *Synergy Between Lithium Plasma-Facing Component Coatings and the Snowflake Divertor Configuration in NSTX*, Paper EX/P3-32, Daejeon (2010).

[56] S. Ding, et al., Plasma Phys. Control. Fusion **52**, 015001 (2010).

[57] A. Bondeson and D.J. Ward, Phys. Rev. Lett. **72**, 2709 (1994).

[58] J. Wesson, *Tokamaks*, Clarendon Press, Oxford, England, 1997.

[59] S.A. Sabbagh, et al., Nuclear Fusion **41**, 1601 (2001).

[60] F. Levinton and H. Yuh, Rev. Sci. Instrum. 79, 10F522 (2008).

[61] B. P. LeBlanc, et al., Rev. Sci. Instrum. **74**, 1659 (2003).

[62] R. J. Hawryluk, et al., "An Empirical Approach to Tokamak Transport", in Physics of Plasmas Close to Thermonuclear Conditions, ed. by B. Coppi, et al., (CEC, Brussels, 1980), Vol. 1, pp. 19-46.

[63] O. Sauter, C. Angioni, and Y.R. Lin-Liu, Phys. Plasmas **6**, 2834 (1999).

[64] A. Pankin, et al., Comput. Phys. Commun. **159**, 157 (2004).

[65] H. Lutjens, et al., Comp. Phys. Comm. **97**, 219 (1996).

[66] A. H. Glasser and M.C. Chance, 1997 *Bull. Am. Phys. Soc.* **42** 1848.

[67] D. A. Gates, et al., Nuclear Fusion **49**, 104016 (2009).

[68] ITER Physics Experts Groups, Nuclear Fusion **39** (1999) 2175.

[69] E. Lazarus, et al., Phys. Plasmas B **3** 2220, (1991).

[70] D. A. Gates, et al., Nuclear Fusion **46**, 17 (2006).

[71] C.E. Kessel, Nuclear Fusion **34**, 1221 (1994).

[72] R.J. Bickerton, J.W. Connor, and J.B. Taylor, Nature (London), Phy. Sci. **229**, 110 (1971).

[73] A. A. Galeev, Sov. Phys. JETP **32**, 752 (1971).

[74] M. C. Zarnstorff and S. C. Prager, Phys. Rev. Lett. **53**, 454 (1984).

[75] A.G. Peeters, Plasma Phys. Control. Fusion **42**, B231 (2000).

[76] T. Ohkawa, Nuclear Fusion **10**, 185 (1970).

[77] N.J. Fisch, Rev. Modern Physics **59**, 175 (1987).

[78] Y.R. Lin-Liu and R.L. Miller, Phys. Plasmas **2**, 1666 (1995).

[79] C.B. Forrest, et al., Phys. Rev. Lett. **73**, 2444 (1994).

[80] S.P. Gerhardt, et al., Nuclear Fusion **51**, 033004 (2011).

[81] J.R. Ferron, et al., Nuclear Fusion **38**, 1055 (1998).

[82] S.P. Gerhardt, et al., *Implementation of β_N Control in the National Spherical Torus Experiment*, accepted for publication in Fusion Science and Technology.

[83] H. Reimerdes, et al., Nuclear Fusion **45**, 369 (2005).

[84] W. Howl, et al., Phys. Fluids B **4**, 1724 (1992).

[85] E. Lazarus, et al., Phys. Rev. Lett **77**, 2714 (1996).

[86] S. A. Sabbagh et al., Proceedings of the 16th International Conference on Fusion Energy, Montreal, CA, 7-11 1996 (1996) AP2-17.

[87] J.R. Ferron, et al., Phys. Plasmas **12**, 056126 (2005).

[88] S.A. Sabbagh, et al., Nuclear Fusion **44**, 560 (2004).

[89] S.A Sabbagh, et al., *Progress Toward Stabilization of Low Internal Inductance Spherical Torus Plasmas in NSTX*, GI2.00001, APS-DPP Meeting, Chicago (2010).

[90] H. Reimerdes, et al., Nuclear Fusion **13**, 056107 (2006).

[91] D. Stutman, et al., Rev. Sci. Instrum. **70**, 572 (1999).

[92] J.E. Menard, et al., Nuclear Fusion **45**, 539 (2005).

[93] J. Breslau, et al., *Onset and Saturation of a Non-Resonant Internal Mode in NSTX and Implications for AT Modes in ITER*, Paper THS/P2-03, Daejeon (2010).

[94] K.C. Shaing, Phys. Fluids **26**, 3315 (1983).

[95] K.C. Shaing, Phys. Plasmas **10**, 1443 (2003).

[96] W. Zhu, et al., Phys. Rev. Lett **96**, 225002 (2006).

[97] A.J. Cole, C.C. Hegna, and J.D. Callen, Phys. Rev. Lett **99**, 065001 (2007).

[98] A.M. Garofalo, Phys. Rev. Lett. **101**, 195005 (2008).

[99] J.-K. Park, et al, Phys. Rev. Lett **102**, 065002 (2009).

[100] S.P. Gerhardt, et al., Nuclear Fusion **49**, 032003 (2009).

[101] T.C. Hender, et al., Nuclear Fusion **44**, 788 (2004).

[102] I.T. Chapman, et al., Nuclear Fusion **50**, 045007.

[103] D. Stutman, et al., Phys. Plasmas **13**, 092511 (2006).

[104] F. M. Levinton, et al., Phys. Plasmas **14**, 056119 (2007).

[105] H.Y. Yuh, et al., Phys. Plasmas **16**, 056120 (2009).

[106] J.R. Ferron, et al. *Optimization of the Safety Factor Profile for High Noninductive Current Fraction Discharges in DIII-D*, Paper EXS/P2-06, Daejeon (2010).

[107] R. Maingi, et al., Phys. Rev. Lett. **105**, 135004 (2010).

[108] A. Loarte, et al., Nuclear Fusion **47**, S203 (2007).

[109] V. A. Soukhanovskii, et al., *High flux expansion divertor studies in NSTX*, 36th EPS Conference on Plasma Physics, Sofia, Bulgaria, 07/29/2009-07/03/2009, *Europhys. Conf. Abstr.*, P2.178, http://arxiv.org/pdf/0912.4281

[110] V.A. Soukhanovskii et al., *'Snowflake' divertor configuration in NSTX*, Journal of Nuclear Materials, In Press, DOI:10.1016/j.jnucmat.2010.07.047.(http://www.sciencedirect.com/science/article/B6TXN-50RP26H2/2/57ab9fb5bcf9688e5d9cb155fc49c9eb)

[111] V.A Soukhanovskii, et al., Nuclear Fusion **51**, 012001 (2011).

[112] D. Ryutov, Phys. Plasmas **14**, 64502 (2007).

[113] D. Ryutov, et al., Phys. Plasmas **15**, 092501 (2008).

[114] J.E. Menard, et al., *Physics Design of NSTX Upgrade*, 37th European Physical Society Conference on Plasma Physics, Dublin, Ireland, online: http://ocs.ciemat.es/EPS2010PAP/pdf/P2.106.pdf

[115] J.W. Berkery, et al., Phys. Rev. Lett. **104**, 035003 (2010).

[116] J.W. Berkery, et al., Phys. Plasmas **17**, 082504 (2010).

[117] D.R. Smith, et al., Phys. Rev. Lett. **102**, 225005 (2009).

[118] D.R. Smith, et al, Phys. Plasmas **16**, 112507 (2009).

[119] K. L. Wong, et al., Phys. Rev. Lett. **99**, 135003 (2007).

[120] K. L. Wong, et al., Phys. Plasmas **15**, 056108 (2008).

[121] W. Guttenfelder, et al., Phys. Rev. Lett. **106**, 155004 (2011).

[122] D. Stutman, et al., Phys. Rev. Lett. **102**, 115002 (2009).

[123] E.D. Fredrickson, et al., Phys. Plasmas **13**, 056109 (2006).

[124] M. Podesta, et al., Phys. Plasmas **16**, 056104 (2009).

[125] E. D. Fredrickson, et al., Phys. Plasmas **16**, 122505 (2009).

[126] K.L. Wong, et al., Phys. Rev. Lett **93**, 085002 (2004).

[127] K. L. Wong, et al., Nuclear Fusion **45**, 30 (2005).

The Princeton Plasma Physics Laboratory is operated
by Princeton University under contract
with the U.S. Department of Energy.

Information Services
Princeton Plasma Physics Laboratory
P.O. Box 451
Princeton, NJ 08543

Phone: 609-243-2245
Fax: 609-243-2751
e-mail: pppl_info@pppl.gov
Internet Address: http://www.pppl.gov